



# Multiscale modeling of cancellous bone considering full coupling of mechanical, electric and magnetic effects

Mischa Blaszczyk<sup>1</sup> · Klaus Hackl<sup>1</sup>

Received: 9 June 2021 / Accepted: 25 September 2021 / Published online: 15 October 2021  
© The Author(s) 2021

## Abstract

Modeling of cancellous bone has important applications in the detection and treatment of fatigue fractures and diseases like osteoporosis. In this paper, we present a fully coupled multiscale approach considering mechanical, electric and magnetic effects by using the multiscale finite element method and a two-phase material model on the microscale. We show numerical results for both scales, including calculations for a femur bone, comparing a healthy bone to ones affected by different stages of osteoporosis. Here, the magnetic field strength resulting from a small mechanical impact decreases drastically for later stages of the disease, confirming experimental research.

**Keywords** Cancellous bone · Multiscale modeling · Coupled problems · Maxwell equations · Wave propagation

## 1 Introduction

In the present contribution, we develop a multiscale model for cancellous bone taking mechanical, electric and magnetic effects into account. An important application of this model is the early detection of osteoporosis. This bone disease reduces the mass density of the bone, making it thinner and weaker, increasing the likelihood of fractures. Sonography is used as a cheap, fast and non-invasive early detection technique for osteoporosis (Kaufman et al. 2008). Material modeling and numerical simulations are helpful tools in order to understand and evaluate experimental measurements and enable medical diagnostics based on this method.

Bone is a composite material with impressive properties, drawing the interest of researchers of many different fields. As a material, it is very strong and stiff and has a high fracture toughness, while also maintaining a light weight (Hamed et al. 2010). Thus in recent decades, a lot of different approaches to investigate and simulate the material behavior of bone have appeared. Many analytical solutions are based on Biot's famous theory (Biot 1956a, b). Examples

include (Buchanan and Gilbert 2007; Chen et al. 2018; Steeb 2010). Here, cortical bone is modeled as a solid, while bone marrow is assumed to be a fluid. The acoustic properties of bone material are then used to obtain mechanical material parameters of bone and the parameters of Biot's model. Additionally, the results are compared with the findings of experiments.

In contrast to the analytical solutions, many numerical approaches exist in the scope of bone modeling as well. The finite difference method was used in Kaufman et al. (2008) to obtain numerical results of ultrasound propagation in bone. Applications of the finite element method (FEM) on the topic of bone modeling include the simulation of mechanical properties of bone (Gardner et al. 2000; Miller et al. 2002) and the simulation of osteogenic effects (Wang et al. 2017). In Christen et al. (2010), patient-specific FEM simulations are proposed in order to estimate the likelihood of osteoporotic fractures.

Since the bone microstructure is very complex and heterogenous, material modeling should take place on different scales. Currently used single-scale models are criticized in Christen et al. (2010) as oversimplified and multiscale approaches are proposed instead. In Hamed et al. (2010), the mechanical properties of bone are modeled on five different length scales from the nanoscale to the macroscale. Multiscale approaches can also be combined with numerical methods. The finite element square method (FE<sup>2</sup>) extends the standard FEM approach by

✉ Mischa Blaszczyk  
mischa.blaszczyk@rub.de

Klaus Hackl  
klaus.hackl@rub.de

<sup>1</sup> Institute of Mechanics of Materials, Ruhr-Universität Bochum, 44801 Bochum, Germany

applying the multiscale concept and solving the differential equation systems on two scales via the FEM. An overview of the method can be found in Schröder (2000); Schröder and Hackl (2013). Basic works on this method include for example (Willis 1981; Suquet 1987; Castañeda and Suquet 1997) and applications to different materials can be found for example in Ilić and Hackl (2004); Miehe et al. (2002). An application of the  $FE^2$  within the scope of bone modeling can be found in Ural and Mischinski (2013); Podshivalov et al. (2011); Pahr and Zysset (2008), proposing different models to capture the microstructure of bone, allowing to investigate mechanical effects. In Ilic et al. (2010) and Klinge et al. (2013), macroscopic material parameters were recovered by simulations on the microscale. The results obtained were subsequently used for macroscale simulations of wave propagation.

So far, all presented contributions focus only on the mechanical effects of bone. However, cortical bone possesses the properties of a piezoelectric solid. After the discovery of this effect (Fukada and Yasuda 1957; Shamos et al. 1963), research considering these coupled physical effects has started. A review on computer modeling of bone piezoelectricity can be found in Mohammadkhah et al. (2019). There, applications are discussed as well. Since electric and magnetic effects are coupled physically via the Maxwell equations, it may be necessary to include magnetic effects as well. In Güzelsu and Saha (1981), bone was modeled as a hollow cylinder and analytical solutions of the coupled equations of all three effects were studied. The results were then compared to in vitro experimental measurements.

In this work, we present a fully coupled multiscale approach for modeling cancellous bone considering mechanical, electric and magnetic effects and using two scales, the macro- and microscale. At the microscale, we assume a heterogeneous material consisting of two phases, cortical bone and bone marrow. Cortical bone is modeled as piezoelectric, insulating solid, bone marrow as viscoelastic, conducting solid. Electric and magnetic effects are coupled via the Maxwell equations. Based on energy methods in mechanics, we establish a thermodynamically consistent material model and derive the weak and strong form of the corresponding boundary value problem. We apply the FEM to solve the problem numerically. For multiscale analysis, we resort to the  $FE^2$  method. To apply this method, we constructed a periodic representative volume element (RVE) and discuss the transition between scales.

The article is structured as follows: in Sect. 2 we discuss the material structure of cancellous bone and the  $FE^2$  method. Then, we introduce the microscopic material model and derive the weak and strong form of the corresponding variational problem. Additionally, we cover the macroscale boundary value problem. In Sect. 3 we present the FEM implementation of the model and show details

regarding scale transition and programming. In Sect. 4 we present numerical results, starting with microscale calculations, on to multiscale simulations for a cylindrical body and finally a true to scale model of a human femur bone. To close this article, we draw a short conclusion and give an outlook to future research envisioned in Sect. 5.

## 2 Material model

### 2.1 Structure and properties of cancellous bone

Our work focuses on the description of the internal structure of cancellous (spongy) bone, which consists of small beams or shells of interconnected cortical bone and interstitial bone marrow. Cortical bone is mainly composed of elastic collagen fibers, which act as charge carriers. When applying a shear stress, these collagen fibers slip past each other, thus producing a piezoelectric effect. This was first measured in Fukada and Yasuda (1957) and later validated in Shamos et al. (1963). This means that, whenever a mechanical strain is present in the bone, an electric field is generated due to the piezoelectric effect. A time-dependent fluctuation of the electric field then creates a magnetic field due to Ampère's circuital law, coupling mechanical, electric and magnetic effects all together.

An important application of bone modeling is the early detection of osteoporosis, a bone disease, which manifests itself in the reduction of the cortical bone phase, thus reducing the strength of the bone and increasing the likelihood of fractures. Compared to a healthy bone, the volume fraction of cortical bone for an affected bone can be reduced from 30 to 5% (Steeb 2010; Ilic et al. 2010). Figure 1 shows a comparison depending on the osteoporosis stage and illustrates the heterogeneity of the material. During the course of osteoporosis, the cortical bone (represented brighter) reduces and is replaced by bone marrow (represented in dark). Thus, we will employ different RVEs for the simulations. Here, the cortical bone phase is represented in gray, while the bone marrow phase is drawn in transparent red color.

Early detection of osteoporosis can be done via sonography: ultrasonic waves enter the bone and due to the described effects create a magnetic field, which can be measured (Güzelsu and Saha 1981) and—depending on the results—conclusions on the health status of the investigated bone can be drawn. In this contribution, we introduce a material model including all the described effects. It is important to note, that there are two different forms of coupling: while the piezoelectric coupling is captured via a suitable material model, the Maxwell coupling is of physical (electrodynamical) nature.

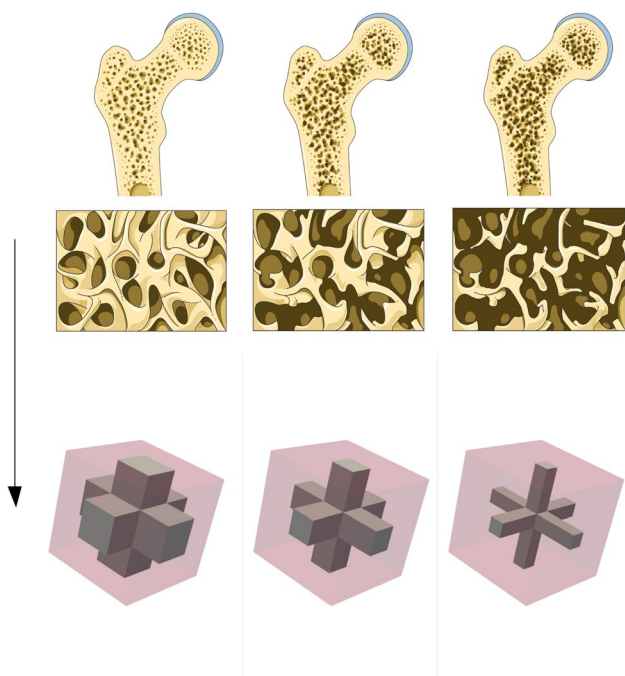


Fig. 1 Bone phases depending on osteoporosis stage (cf. Laboratoires 2019) and corresponding RVEs

### 2.2 Concept of the FE<sup>2</sup> method

To include micro-heterogeneities directly, an extremely fine resolution of the problem would be necessary, resulting in a very high computation cost for the simulations. Alternatively, the FE<sup>2</sup> method is a homogenization technique, which captures the structure of micro-heterogeneities by introducing a second—smaller—scale to the problem. If the material is statistically regular on the smaller scale, it can be modeled by a corresponding RVE (Schröder 2000; Schröder and Hackl 2013). In this paper, we denote the larger scale as the macroscale and the smaller scale as the microscale. To obtain accurate results, the quotient of the characteristic lengths between micro- and macroscale should tend to zero, so the RVE has to be much smaller than the simulated macroscopic body. Figure 2 illustrates this procedure: instead of using a material model on the macroscale, the state variables are linked to the microscale, where the RVE problem is solved. The microscale calculations yield average flux quantities and consistent tangent matrices, which then can be used for the solution of the macroscale problem, replacing a macroscopic material model.

We denote spatial coordinates on the macroscale by  $\mathbf{x}$  and on the microscale by  $\mathbf{y}$ . Quantities denoted as  $(\cdot)$  are affiliated to the macroscale. The transition between the scales regarding energy conservation and numerical treatment is discussed in Sect. 3.2.

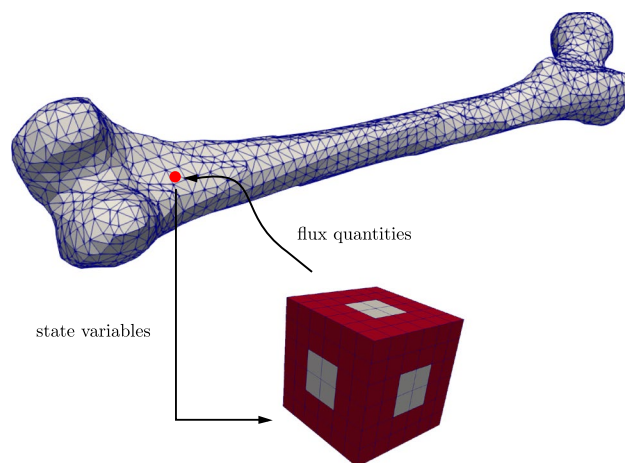


Fig. 2 Transition between macro- and microscale. State variables enter as boundary conditions of the RVE problem. Flux quantities at the macroscale are calculated by averaging the RVE quantities

### 2.3 Variational formulation of the microscale problem

The domain  $\Omega := \Omega_y$ , representing the RVE of the micro-problem, is split into a cortical bone part  $\Omega_b$  and a bone marrow part  $\Omega_m$ . For any quantity, the indices  $(\cdot)_m$  and  $(\cdot)_b$  are used to denote the affiliation to each phase. If no index is present, the quantity or equation is valid for both phases. We employ the following thermodynamic energy functional at the microscale:

$$\begin{aligned} \Pi = & \int_{\Omega_b} \Psi_b(\boldsymbol{\varepsilon}, \mathbf{E}, \mathbf{B}) dV + \int_{\Omega_m} \Psi_m(\boldsymbol{\varepsilon}, \boldsymbol{\varepsilon}^i, \mathbf{E}, \mathbf{B}) + \mathcal{C} dV \\ & + \int_{\Omega_m} \int_t \Delta(\dot{\boldsymbol{\varepsilon}}^i, \dot{\mathbf{A}}) dt dV + \int_{\Omega} \Psi_g(\nabla \cdot \mathbf{A}) dV - W_{\text{ext}} . \end{aligned} \tag{1}$$

The functional contains the energy densities  $\Psi_b$  and  $\Psi_m$  of both phases, a volume constraint  $\mathcal{C}$ , dissipation and gauge functionals ( $\Delta$  and  $\Psi_g$ ) and the potential of the generalized external forces  $W_{\text{ext}}$ . The main variables of the problem are then the mechanical displacements  $\mathbf{u}$ , the electric scalar potential  $\varphi$  and the magnetic vector potential  $\mathbf{A}$ , yielding seven unknown variables for the three-dimensional model. The state variables are the mechanical strain  $\boldsymbol{\varepsilon}$ , the electric field  $\mathbf{E}$  and the magnetic flux density  $\mathbf{B}$ , calculated as

$$\boldsymbol{\varepsilon} = \frac{1}{2} (\nabla \mathbf{u} + \nabla^T \mathbf{u}) , \mathbf{E} = -\nabla \varphi - \dot{\mathbf{A}} \text{ and } \mathbf{B} = \nabla \times \mathbf{A} . \tag{2}$$

This way, two of the four Maxwell equations are already satisfied:

$$\begin{aligned} \nabla \times \mathbf{E} &= \nabla \times (-\nabla \varphi - \dot{\mathbf{A}}) = -\dot{\mathbf{B}} \quad \text{and} \\ \nabla \cdot \mathbf{B} &= \nabla \cdot (\nabla \times \mathbf{A}) = \mathbf{0}. \end{aligned} \tag{3}$$

For the mechanical strain, we use Voigt’s notation (Mehrabadi and Cowin 1990) as

$$\boldsymbol{\varepsilon} = (\varepsilon_{xx} \ \varepsilon_{yy} \ \varepsilon_{zz} \ 2\varepsilon_{xy} \ 2\varepsilon_{yz} \ 2\varepsilon_{xz})^T. \tag{4}$$

Then, the energy densities for both phases are

$$\begin{aligned} \Psi_b &= \frac{1}{2} (\boldsymbol{\varepsilon} \cdot \mathbf{C}_b \cdot \boldsymbol{\varepsilon} - \mathbf{E} \cdot \boldsymbol{\xi}_b \cdot \mathbf{E} + \mathbf{B} \cdot \boldsymbol{\mu}_b^{-1} \cdot \mathbf{B}) \\ &\quad - \mathbf{e}_b \cdot \boldsymbol{\varepsilon} \cdot \mathbf{E} \quad \text{and} \\ \Psi_m &= \frac{1}{2} ((\boldsymbol{\varepsilon} - \boldsymbol{\varepsilon}^i) \cdot \mathbf{C}_m \cdot (\boldsymbol{\varepsilon} - \boldsymbol{\varepsilon}^i) - \mathbf{E} \cdot \boldsymbol{\xi}_m \cdot \mathbf{E} \\ &\quad + \mathbf{B} \cdot \boldsymbol{\mu}_m^{-1} \cdot \mathbf{B}), \end{aligned} \tag{5}$$

consisting of quadratic energies for mechanical, electric and magnetic effects, resulting in a linear problem. We include a piezoelectric energy term for the cortical bone phase. For the bone marrow phase, an inelastic strain  $\boldsymbol{\varepsilon}^i$  is introduced. Here,  $\mathbf{C}$  is the mechanical stiffness tensor,  $\boldsymbol{\xi}$  is the permittivity tensor,  $\boldsymbol{\mu}^{-1}$  is the inverse permeability tensor and  $\mathbf{e}_b$  is the piezoelectric tensor. While it is possible to switch between state and flux variables via a Legendre transformation, the present formulation proves as the most suitable for our model, as it allows an easy inclusion of the Maxwell coupling and the electric dissipation. For linear problems, the transformation would change an extremal into a saddle point problem, thus excluding solvers, that require positive definiteness of the system matrix as a precondition. The constraint function reads

$$\mathcal{C} = \lambda \operatorname{tr}(\boldsymbol{\varepsilon}^i), \tag{6}$$

enforcing volume conservation of the inelastic deformation. Here,  $\lambda$  is a Lagrange multiplier. The dissipation function is

$$\Delta = \frac{1}{2} (\boldsymbol{\mu}_v^{-1} |\dot{\boldsymbol{\varepsilon}}^i|^2 - \boldsymbol{\kappa} \mathbf{E}^2), \quad \text{with} \quad \mathbf{J} = \boldsymbol{\kappa} \mathbf{E}. \tag{7}$$

Thus,  $\Delta$  governs the evolution of the inelastic strain and the energy loss due to conduction. The latter satisfies Ohm’s law (Eq. (7), right). Both parts of the dissipation only occur in the bone marrow phase. Here, the viscosity parameter  $\boldsymbol{\mu}_v^{-1} > 0$ , the electric conductivity tensor  $\boldsymbol{\kappa} = \kappa_1 \mathbf{I}$ , with the identity tensor  $\mathbf{I}$ , the electric conductivity  $\kappa_1 > 0$  and the electric current density  $\mathbf{J}$  are introduced. The gauge function is

$$\Psi_g = \frac{\gamma}{2} (\nabla \cdot \mathbf{A})^2 \tag{8}$$

and ensures, that a unique solution for the magnetic vector potential  $\mathbf{A}$  is obtained by penalizing its divergence, effectively requiring, that  $\nabla \cdot \mathbf{A}$  vanishes and thus improving the

numerical stability (Semenov et al.2006). The penalty parameter  $\gamma$  is a numerical parameter used to control the gauge term. Finally, the potential of generalized external forces is

$$\begin{aligned} W_{\text{ext}} &= \int_{\Omega} (\mathbf{f} \cdot \mathbf{u} - q_v \cdot \varphi + \mathbf{j}_v \cdot \mathbf{A}) dV \\ &\quad + \int_{\partial\Omega} (\mathbf{t} \cdot \mathbf{u} - q_s \cdot \varphi + \mathbf{j}_s \cdot \mathbf{A}) dA. \end{aligned} \tag{9}$$

Here,  $\mathbf{f}$  and  $\mathbf{t}$  are the mechanical volume and surface forces,  $q_v$  and  $q_s$  are the electric volume and surface charges and  $\mathbf{j}_v$  and  $\mathbf{j}_s$  are the volume and surface currents.

By calculating the derivative of the energy density with respect to the state variables, we find the following constitutive equations for both phases:

$$\begin{aligned} \boldsymbol{\sigma} &:= \frac{\partial \Psi_b}{\partial \boldsymbol{\varepsilon}} = \mathbf{C}_b \cdot \boldsymbol{\varepsilon} - \mathbf{e}_b^T \cdot \mathbf{E}, \\ \mathbf{D} &:= -\frac{\partial \Psi_b}{\partial \mathbf{E}} = \mathbf{e}_b \cdot \boldsymbol{\varepsilon} + \boldsymbol{\xi}_b \cdot \mathbf{E}, \\ \mathbf{H} &:= \frac{\partial \Psi_b}{\partial \mathbf{B}} = \boldsymbol{\mu}_b^{-1} \cdot \mathbf{B}, \end{aligned} \tag{10}$$

$$\begin{aligned} \boldsymbol{\sigma} &:= \frac{\partial \Psi_m}{\partial \boldsymbol{\varepsilon}} = \mathbf{C}_m \cdot (\boldsymbol{\varepsilon} - \boldsymbol{\varepsilon}^i), \\ \mathbf{D} &:= -\frac{\partial \Psi_m}{\partial \mathbf{E}} = \boldsymbol{\xi}_m \cdot \mathbf{E} \quad \text{and} \\ \mathbf{H} &:= \frac{\partial \Psi_m}{\partial \mathbf{B}} = \boldsymbol{\mu}_m^{-1} \cdot \mathbf{B}. \end{aligned}$$

For the bone marrow, the additional constitutive equations are

$$\begin{aligned} \boldsymbol{\sigma} &:= -\frac{\partial \Psi_m}{\partial \boldsymbol{\varepsilon}^i} = \mathbf{C}_m \cdot (\boldsymbol{\varepsilon} - \boldsymbol{\varepsilon}^i) \quad \text{and} \\ \mathbf{J} &:= \frac{\partial \Delta}{\partial \mathbf{E}} = -\frac{\partial \Delta}{\partial \dot{\mathbf{A}}} = \boldsymbol{\kappa}_m \mathbf{E}, \end{aligned} \tag{11}$$

introducing the flux quantities mechanical stress  $\boldsymbol{\sigma}$ , electric displacement  $\mathbf{D}$  and magnetic field strength  $\mathbf{H}$ . For the cortical bone phase, the viscosity parameter  $\boldsymbol{\mu}_v^{-1}$  and the electric conductivity tensor  $\boldsymbol{\kappa}$  vanish. The material tensors satisfy

$$\begin{aligned} \mathbf{C} &:= \frac{\partial \boldsymbol{\sigma}}{\partial \boldsymbol{\varepsilon}}, & \boldsymbol{\xi} &:= \frac{\partial \mathbf{D}}{\partial \mathbf{E}}, & \mathbf{e} &:= \frac{\partial \mathbf{D}}{\partial \boldsymbol{\varepsilon}} = -\left(\frac{\partial \boldsymbol{\sigma}}{\partial \mathbf{E}}\right)^T, \\ \boldsymbol{\mu}^{-1} &:= \frac{\partial \mathbf{H}}{\partial \mathbf{B}}, & \boldsymbol{\kappa} &:= \frac{\partial \mathbf{J}}{\partial \mathbf{E}}. \end{aligned} \tag{12}$$

### 2.4 Weak and strong form of the microscale problem

To calculate the weak and strong form of the problem, the energy functional has to become stationary with respect to the main variables and internal variables, leading to

$$\int_{t_0}^{t_1} \Pi \, dt \rightarrow \underset{\mathbf{u}, \varphi, \mathbf{A}, \varepsilon^i}{stat} . \tag{13}$$

The stationary condition of the first variation of the energy functional reads then

$$\begin{aligned} & \int_{\Omega_b} \left( \frac{\partial \Psi_b}{\partial \varepsilon} \delta \varepsilon + \frac{\partial \Psi_b}{\partial \mathbf{E}} \delta \mathbf{E} + \frac{\partial \Psi_b}{\partial \mathbf{B}} \delta \mathbf{B} \right) dV \\ & + \int_{\Omega_m} \left( \frac{\partial \Psi_m}{\partial \varepsilon} \delta \varepsilon + \frac{\partial \Psi_m}{\partial \varepsilon^i} \delta \varepsilon^i + \frac{\partial \Psi_m}{\partial \mathbf{E}} \delta \mathbf{E} \right. \\ & + \frac{\partial \Psi_m}{\partial \mathbf{B}} \delta \mathbf{B} + \frac{\partial \Delta}{\partial \dot{\varepsilon}^i} \delta \varepsilon^i + \frac{\partial \Delta}{\partial \dot{\mathbf{A}}} \delta \dot{\mathbf{A}} \\ & \left. + \lambda \mathbf{I} \delta \varepsilon^i \right) dV + \int_{\Omega} \frac{\partial \Psi_g}{\partial (\nabla \cdot \mathbf{A})} \\ & \delta (\nabla \cdot \mathbf{A}) dV - \delta W_{ext} = \delta \Pi = 0 \quad \forall \delta \mathbf{u}, \delta \varphi, \delta \mathbf{A}, \delta \varepsilon^i . \end{aligned} \tag{14}$$

The variation of the generalized external forces is

$$\begin{aligned} \delta W_{ext} = & \int_{\Omega} (\mathbf{f} \cdot \delta \mathbf{u} - q_v \cdot \delta \varphi + \mathbf{j}_v \cdot \delta \mathbf{A}) dV \\ & + \int_{\partial \Omega} (\mathbf{t} \cdot \delta \mathbf{u} - q_s \cdot \delta \varphi + \mathbf{j}_s \cdot \delta \mathbf{A}) dA . \end{aligned} \tag{15}$$

Using the introduced energy densities, constraint, dissipation and gauge functions, Eqs. (5), (6), (7), (8), and inserting the constitutive equations Eqs. (10), (14) simplifies to

$$\begin{aligned} & \int_{\Omega} (\boldsymbol{\sigma} \cdot \delta \varepsilon - \mathbf{D} \cdot \delta \mathbf{E} + \mathbf{H} \cdot \delta \mathbf{B} - \mathbf{J} \cdot \delta \mathbf{A} \\ & + \gamma (\nabla \cdot \mathbf{A}) \cdot \delta (\nabla \cdot \mathbf{A}) + (-\boldsymbol{\sigma} + \mu_v^{-1} \dot{\varepsilon}^i + \lambda \mathbf{I}) \\ & \delta \varepsilon^i) dV - \delta W_{ext} = 0 \quad \forall \delta \mathbf{u}, \delta \varphi, \delta \mathbf{A}, \delta \varepsilon^i . \end{aligned} \tag{16}$$

Here, the identity vector is denoted as  $\mathbf{I}$ . We find the evolution equation of the inelastic strain:

$$-\boldsymbol{\sigma} + \mu_v^{-1} \dot{\varepsilon}^i + \lambda \mathbf{I} = \mathbf{0} . \tag{17}$$

To calculate the Lagrange multiplier, the trace is applied to Eq. (17):

$$-\text{tr}(\boldsymbol{\sigma}) + \underbrace{\mu_v^{-1} \text{tr}(\dot{\varepsilon}^i)}_{=0} + \lambda \text{tr}(\mathbf{I}) = 0 \Rightarrow \lambda = \frac{1}{3} \text{tr}(\boldsymbol{\sigma}) . \tag{18}$$

The second term in Eq. (18) must vanish because of the introduced volume constraint. This leads to the final evolution equation

$$\dot{\varepsilon}^i = \mu_v \boldsymbol{\sigma}_{dev} , \tag{19}$$

with  $\boldsymbol{\sigma}_{dev} = \boldsymbol{\sigma} - \frac{1}{3} \text{tr}(\boldsymbol{\sigma}) \mathbf{I}$  denoting the deviatoric part of the mechanical stress  $\boldsymbol{\sigma}$ . The time integration of the evolution equation is discussed in Sect. 3.

To calculate the strong form of the problem, the remaining variational equation is used:

$$\begin{aligned} & \int_{\Omega} (\boldsymbol{\sigma} \cdot \delta \varepsilon - \mathbf{D} \cdot \delta \mathbf{E} + \mathbf{H} \cdot \delta \mathbf{B} - \mathbf{J} \cdot \delta \mathbf{A} \\ & + \gamma (\nabla \cdot \mathbf{A}) \cdot \delta (\nabla \cdot \mathbf{A})) dV - \delta W_{ext} = 0 \quad \forall \delta \mathbf{u}, \delta \varphi, \delta \mathbf{A} . \end{aligned} \tag{20}$$

This form is later used to insert a FEM ansatz. We apply partial integration to each term. Details can be found in Appendix A. We obtain

$$\begin{aligned} \nabla \cdot \boldsymbol{\sigma} + \mathbf{f} &= \mathbf{0} \quad \text{in } \Omega \\ \boldsymbol{\sigma} \cdot \mathbf{n} &= \mathbf{t} \quad \text{on } \partial \Omega \\ \nabla \cdot \mathbf{D} &= q_v \quad \text{in } \Omega \\ \mathbf{D} \cdot \mathbf{n} &= -q_s \quad \text{on } \partial \Omega \\ \nabla \times \mathbf{H} &= \dot{\mathbf{D}} + \mathbf{J} + \gamma \nabla (\nabla \cdot \mathbf{A}) + \mathbf{j}_v \quad \text{in } \Omega \\ \mathbf{H} \times \mathbf{n} &= \mathbf{j}_s - \gamma (\nabla \cdot \mathbf{A}) \mathbf{n} \quad \text{on } \partial \Omega \end{aligned} \tag{21}$$

recovering the mechanical equilibrium condition, the two remaining Maxwell equations and boundary conditions, including the gauge. Here,  $\mathbf{n}$  is the normal vector pointing outwards. Additionally, we receive the jump conditions between the phases

$$\begin{aligned} & ]_{bm} \cdot \mathbf{n} = \mathbf{t} \quad \text{on } \partial \Omega_{bm} \\ & [[\mathbf{D}]]_{bm} \cdot \mathbf{n} = -q_s \quad \text{on } \partial \Omega_{bm} \\ & [[\mathbf{H}]]_{bm} \times \mathbf{n} = \mathbf{j}_s - \gamma [[\nabla \cdot \mathbf{A}]]_{bm} \mathbf{n} \quad \text{on } \partial \Omega_{bm} \end{aligned} \tag{22}$$

on the interface  $\partial \Omega_{bm}$  and the evolution equation of the inelastic strain Eq. (19) in  $\Omega_m$ . Here  $[[\cdot]]_{12} := (\cdot)_1 - (\cdot)_2$  denotes the difference between the phases. It should be noted that the strong form is valid for both phases, but the calculation of the flux variables and the inelastic strain evolution depends on the specific material parameters and thus in which phase the calculation is done.

### 2.5 Macroscale problem

For the macroscale, the following boundary value problem in the domain  $\Omega_x$  has to be solved: find the set  $\{\bar{\mathbf{u}}, \bar{\varphi}, \bar{\mathbf{A}}\}$ , such that



$$\begin{aligned}
 \nabla \cdot \bar{\boldsymbol{\sigma}} + \bar{\mathbf{f}} &= \mathbf{0} \quad \text{in } \Omega_x \\
 \bar{\boldsymbol{\sigma}} \cdot \mathbf{n} &= \bar{\mathbf{t}} \quad \text{on } \partial\Omega_x \\
 \nabla \cdot \bar{\mathbf{D}} &= \bar{q}_v \quad \text{in } \Omega_x \\
 \bar{\mathbf{D}} \cdot \mathbf{n} &= -\bar{q}_s \quad \text{on } \partial\Omega_x \\
 \nabla \times \bar{\mathbf{H}} &= \bar{\mathbf{D}} + \bar{\mathbf{J}} + \gamma \nabla(\nabla \cdot \bar{\mathbf{A}}) + \bar{\mathbf{j}}_v \quad \text{in } \Omega_x \\
 \bar{\mathbf{H}} \times \mathbf{n} &= \bar{\mathbf{j}}_s - \gamma(\nabla \cdot \bar{\mathbf{A}})\mathbf{n} \quad \text{on } \partial\Omega_x,
 \end{aligned}
 \tag{23}$$

with the state variables

$$\bar{\boldsymbol{\varepsilon}} = \frac{1}{2}(\nabla \bar{\mathbf{u}} + \nabla^T \bar{\mathbf{u}}), \quad \bar{\mathbf{E}} = -\nabla \bar{\varphi} - \dot{\bar{\mathbf{A}}} \quad \text{and} \quad \bar{\mathbf{B}} = \nabla \times \bar{\mathbf{A}}, \tag{24}$$

and the calculation of the fluxes depending on the microscale calculations

$$(\bar{\boldsymbol{\sigma}}, \bar{\mathbf{D}}, \bar{\mathbf{H}}, \bar{\mathbf{J}}) = f_{\text{RVE}}(\bar{\boldsymbol{\varepsilon}}, \bar{\mathbf{E}}, \bar{\mathbf{B}}). \tag{25}$$

We transform the strong form into the weak form by multiplying with test functions of the main variables and again using partial integration:

$$\begin{aligned}
 \int_{\Omega_x} (\bar{\boldsymbol{\sigma}} \cdot \delta \bar{\boldsymbol{\varepsilon}} - \bar{\mathbf{D}} \cdot \delta \bar{\mathbf{E}} + \bar{\mathbf{H}} \cdot \delta \bar{\mathbf{B}} - \bar{\mathbf{J}} \cdot \delta \bar{\mathbf{A}} \\
 + \gamma(\nabla \cdot \bar{\mathbf{A}}) \cdot \delta(\nabla \cdot \bar{\mathbf{A}})) dV - \delta \bar{W}_{\text{ext}} = 0 \quad \forall \delta \bar{\mathbf{u}}, \delta \bar{\varphi}, \delta \bar{\mathbf{A}}.
 \end{aligned}
 \tag{26}$$

Here, the variation of the macroscopic generalized external forces is

$$\begin{aligned}
 \delta \bar{W}_{\text{ext}} &= \int_{\Omega_x} (\bar{\mathbf{f}} \cdot \delta \bar{\mathbf{u}} - \bar{q}_v \cdot \delta \bar{\varphi} + \bar{\mathbf{j}}_v \cdot \delta \bar{\mathbf{A}}) dV \\
 &+ \int_{\partial\Omega_x} (\bar{\mathbf{t}} \cdot \delta \bar{\mathbf{u}} - \bar{q}_s \cdot \delta \bar{\varphi} + \bar{\mathbf{j}}_s \cdot \delta \bar{\mathbf{A}}) dA.
 \end{aligned}
 \tag{27}$$

This form is again used in the next section to formulate the FEM.

### 3 Numerical implementation

#### 3.1 Finite element method

To solve the boundary value problems on both scales, we insert a standard finite element approach (Zienkiewicz et al. 2005) into the weak form of the problem for all main variables. In this section, we derive the resulting system for the microscale. It should be noted that the same system has to be solved for the macroscale, but each quantity  $(\cdot)$  has to be replaced by its macro-average quantity  $(\hat{\cdot})$ . The inelastic strain is only present on the microscale and

vanishes on the macroscale. Its calculation is not done via the FEM, but directly by using the evolution equation Eq. (19) on the integration point level. Details regarding the calculation of macro-fluxes and consistent material tensors are given in the next subsection. Here, we denote nodal FEM values by  $(\hat{\cdot})$ . For the evolution equation of the inelastic strain on the micro-scale, we apply an explicit Euler scheme, yielding:

$$\boldsymbol{\varepsilon}_{n+1}^i = \boldsymbol{\varepsilon}_n^i + \Delta t \dot{\boldsymbol{\varepsilon}}^i \quad \text{with} \quad \dot{\boldsymbol{\varepsilon}}^i = \mu_v \boldsymbol{\sigma}_{\text{dev}}. \tag{28}$$

Here,  $\Delta t$  is the time increment between two time steps. The standard FEM approach for the remaining system is

$$\begin{aligned}
 \mathbf{u} &\approx \mathbf{N}_u \hat{\mathbf{u}} & \boldsymbol{\varphi} &\approx \mathbf{N}_\varphi \hat{\boldsymbol{\varphi}} & \mathbf{A} &\approx \mathbf{N}_A \hat{\mathbf{A}} \\
 \delta \mathbf{u} &\approx \mathbf{N}_u \delta \hat{\mathbf{u}} & \delta \boldsymbol{\varphi} &\approx \mathbf{N}_\varphi \delta \hat{\boldsymbol{\varphi}} & \delta \mathbf{A} &\approx \mathbf{N}_A \delta \hat{\mathbf{A}}
 \end{aligned}
 \tag{29}$$

approximating the main variable and their variations by shape functions times the nodal values of the functions  $(\cdot) \approx \mathbf{N}(\hat{\cdot})$ . For the state variables and the gauge, this approach yields

$$\begin{aligned}
 \hat{\boldsymbol{\varepsilon}} &= \mathbf{B}_u \hat{\mathbf{u}}, & \hat{\mathbf{E}} &= -\mathbf{B}_{\text{grad}} \hat{\boldsymbol{\varphi}} - \mathbf{N}_A \hat{\mathbf{A}}, \\
 \hat{\mathbf{B}} &= \mathbf{B}_{\text{curl}} \hat{\mathbf{A}}, & \nabla \cdot \hat{\mathbf{A}} &= \mathbf{B}_{\text{div}} \hat{\mathbf{A}}.
 \end{aligned}
 \tag{30}$$

Here, the operator matrices are

$$\begin{aligned}
 \mathbf{B}_u &= \begin{pmatrix} \frac{\partial}{\partial x} & 0 & 0 \\ 0 & \frac{\partial}{\partial y} & 0 \\ 0 & 0 & \frac{\partial}{\partial z} \\ \frac{\partial}{\partial y} & \frac{\partial}{\partial x} & 0 \\ 0 & \frac{\partial}{\partial z} & \frac{\partial}{\partial y} \\ \frac{\partial}{\partial z} & 0 & \frac{\partial}{\partial x} \end{pmatrix} \cdot \mathbf{N}_u \\
 \mathbf{B}_{\text{grad}} &= \begin{pmatrix} \frac{\partial}{\partial x} \\ \frac{\partial}{\partial y} \\ \frac{\partial}{\partial z} \end{pmatrix} \cdot \mathbf{N}_\varphi \\
 \mathbf{B}_{\text{curl}} &= \begin{pmatrix} 0 & \frac{\partial}{\partial z} & -\frac{\partial}{\partial y} \\ -\frac{\partial}{\partial z} & 0 & \frac{\partial}{\partial x} \\ \frac{\partial}{\partial y} & -\frac{\partial}{\partial x} & 0 \end{pmatrix} \cdot \mathbf{N}_A \\
 \mathbf{B}_{\text{div}} &= \begin{pmatrix} \frac{\partial}{\partial x} & \frac{\partial}{\partial y} & \frac{\partial}{\partial z} \end{pmatrix} \cdot \mathbf{N}_A
 \end{aligned}
 \tag{31}$$

Inserting these equations into the reduced weak form of the micro-problem Eq. (20) and by using the arbitrariness of the test functions, we find the final equation system in matrix form as follows (a detailed derivation is given in Appendix B):

$$\mathbf{R} := \mathbf{F} - \mathbf{M}\dot{\mathbf{d}} - \mathbf{C}\mathbf{d} - \mathbf{K}\mathbf{d} \stackrel{!}{=} \mathbf{0} \tag{32}$$

with the residual vector  $\mathbf{R} = (\mathbf{R}_u \ \mathbf{R}_\varphi \ \mathbf{R}_A)^T =$

$$\begin{pmatrix} \hat{\mathbf{f}} + \int_{\Omega} -\mathbf{B}_u^T \hat{\boldsymbol{\sigma}} dV \\ \hat{\mathbf{q}} + \int_{\Omega} -\mathbf{B}_{\text{grad}}^T \hat{\mathbf{D}} dV \\ \hat{\mathbf{j}} + \int_{\Omega} (\mathbf{N}_A^T (\dot{\mathbf{D}} + \hat{\mathbf{J}}) - \mathbf{B}_{\text{curl}}^T \hat{\mathbf{H}} - \gamma \mathbf{B}_{\text{div}} \mathbf{B}_{\text{div}}^T \hat{\mathbf{A}}) dV \end{pmatrix} \quad (33)$$

and the generalized force and displacement vectors together with the mass, damping and stiffness matrices as follows:

$$\begin{aligned} \mathbf{d} &:= \begin{pmatrix} \hat{\mathbf{u}} \\ \hat{\boldsymbol{\phi}} \\ \hat{\mathbf{A}} \end{pmatrix}, \quad \mathbf{F} = \begin{pmatrix} \hat{\mathbf{f}} \\ \hat{\mathbf{q}} \\ \hat{\mathbf{j}} \end{pmatrix}, \\ \mathbf{M} &= \begin{pmatrix} \mathbf{0} & \mathbf{0} & \mathbf{0} \\ \mathbf{0} & \mathbf{0} & \mathbf{0} \\ \mathbf{0} & \mathbf{0} & \mathbf{M}_{AA} \end{pmatrix}, \quad \mathbf{C} = \begin{pmatrix} \mathbf{0} & \mathbf{0} & \mathbf{C}_{uA} \\ \mathbf{0} & \mathbf{0} & \mathbf{C}_{\phi A} \\ \mathbf{C}_{Au} & \mathbf{C}_{A\phi} & \mathbf{C}_{AA} \end{pmatrix}, \\ \mathbf{K} &= \begin{pmatrix} \mathbf{K}_{uu} & \mathbf{K}_{u\phi} & \mathbf{0} \\ \mathbf{K}_{\phi u} & \mathbf{K}_{\phi\phi} & \mathbf{0} \\ \mathbf{0} & \mathbf{K}_{A\phi} & \mathbf{K}_{AA} \end{pmatrix}. \\ \mathbf{K}_{uu} &:= -\frac{\partial \mathbf{R}_u}{\partial \hat{\mathbf{u}}} = \int_{\Omega} \mathbf{B}_u^T \mathbf{C}_{\text{tang}} \mathbf{B}_u dV, \\ \mathbf{K}_{u\phi} &:= -\frac{\partial \mathbf{R}_u}{\partial \hat{\boldsymbol{\phi}}} = \int_{\Omega} \mathbf{B}_u^T \mathbf{e}^T \mathbf{B}_{\text{grad}} dV, \\ \mathbf{K}_{\phi u} &:= -\frac{\partial \mathbf{R}_{\phi}}{\partial \hat{\mathbf{u}}} = \int_{\Omega} \mathbf{B}_{\text{grad}}^T \mathbf{e} \mathbf{B}_u dV, \\ \mathbf{K}_{\phi\phi} &:= -\frac{\partial \mathbf{R}_{\phi}}{\partial \hat{\boldsymbol{\phi}}} = \int_{\Omega} -\mathbf{B}_{\text{grad}}^T \boldsymbol{\xi} \mathbf{B}_{\text{grad}} dV, \\ \mathbf{K}_{AA} &:= -\frac{\partial \mathbf{R}_A}{\partial \hat{\mathbf{A}}} = \int_{\Omega} \mathbf{B}_{\text{curl}}^T \boldsymbol{\mu}^{-1} \mathbf{B}_{\text{curl}} + \gamma \mathbf{B}_{\text{div}} \mathbf{B}_{\text{div}}^T dV, \\ \mathbf{K}_{A\phi} &:= -\frac{\partial \mathbf{R}_A}{\partial \hat{\boldsymbol{\phi}}} = \int_{\Omega} \mathbf{N}_A^T \boldsymbol{\kappa} \mathbf{B}_{\text{grad}} dV, \\ \mathbf{C}_{uA} &:= -\frac{\partial \mathbf{R}_u}{\partial \hat{\mathbf{A}}} = \int_{\Omega} \mathbf{B}_u^T \mathbf{e}^T \mathbf{N}_A dV, \\ \mathbf{C}_{Au} &:= -\frac{\partial \mathbf{R}_A}{\partial \hat{\mathbf{u}}} = \int_{\Omega} -\mathbf{N}_A^T \mathbf{e} \mathbf{B}_u dV, \\ \mathbf{C}_{\phi A} &:= -\frac{\partial \mathbf{R}_{\phi}}{\partial \hat{\mathbf{A}}} = \int_{\Omega} -\mathbf{B}_{\text{grad}}^T \boldsymbol{\xi} \mathbf{N}_A dV, \\ \mathbf{C}_{A\phi} &:= -\frac{\partial \mathbf{R}_A}{\partial \hat{\boldsymbol{\phi}}} = \int_{\Omega} \mathbf{N}_A^T \boldsymbol{\xi} \mathbf{B}_{\text{grad}} dV, \\ \mathbf{C}_{AA} &:= -\frac{\partial \mathbf{R}_A}{\partial \hat{\mathbf{A}}} = \int_{\Omega} \mathbf{N}_A^T \boldsymbol{\kappa} \mathbf{N}_A dV, \\ \mathbf{M}_{AA} &:= -\frac{\partial \mathbf{R}_A}{\partial \hat{\mathbf{A}}} = \int_{\Omega} \mathbf{N}_A^T \boldsymbol{\xi} \mathbf{N}_A dV. \end{aligned} \quad (34)$$

The material tensors depend again on the phase. We calculate the mechanical stiffness tangent matrix  $\mathbf{C}_{\text{tang}}$  by introducing a time discretization as:

$$\mathbf{C}_{\text{tang}} = \frac{\partial \boldsymbol{\sigma}_{n+1}}{\partial \boldsymbol{\varepsilon}_{n+1}} = \begin{cases} \mathbf{C}_b & \text{in } \Omega_b \\ \mathbf{C}_m - \mathbf{C}_m \frac{\partial \boldsymbol{\varepsilon}_{n+1}^i}{\partial \boldsymbol{\varepsilon}_{n+1}} & \text{in } \Omega_m \end{cases} \quad (35)$$

For the bone marrow phase, the calculation depends on the inelastic strain  $\boldsymbol{\varepsilon}_{n+1}^i$ :

$$\frac{\partial \boldsymbol{\varepsilon}_{n+1}^i}{\partial \boldsymbol{\varepsilon}_{n+1}} = \mu_v \frac{\partial \boldsymbol{\sigma}_{\text{dev}}}{\partial \boldsymbol{\sigma}} \underbrace{\frac{\partial \boldsymbol{\sigma}}{\partial \boldsymbol{\varepsilon}_{n+1}}}_{\mathbf{C}_m}, \quad (36)$$

with

$$\begin{aligned} \mathbf{D}_{\text{devd}} &:= \frac{\partial \boldsymbol{\sigma}_{\text{dev}}}{\partial \boldsymbol{\sigma}} = \mathbf{I} - \frac{1}{3} \begin{pmatrix} 1 & 1 & 1 & 0 & 0 & 0 \\ 1 & 1 & 1 & 0 & 0 & 0 \\ 1 & 1 & 1 & 0 & 0 & 0 \\ 0 & 0 & 0 & 0 & 0 & 0 \\ 0 & 0 & 0 & 0 & 0 & 0 \\ 0 & 0 & 0 & 0 & 0 & 0 \end{pmatrix} \\ &= \frac{1}{3} \begin{pmatrix} 2 & -1 & -1 & 0 & 0 & 0 \\ -1 & 2 & -1 & 0 & 0 & 0 \\ -1 & -1 & 2 & 0 & 0 & 0 \\ 0 & 0 & 0 & 3 & 0 & 0 \\ 0 & 0 & 0 & 0 & 3 & 0 \\ 0 & 0 & 0 & 0 & 0 & 3 \end{pmatrix}. \end{aligned} \quad (37)$$

The mechanical stiffness tangent matrix for the bone marrow phase is then

$$\mathbf{C}_{\text{tang}} = \mathbf{C}_m - \mathbf{C}_m (\mu_v \mathbf{D}_{\text{devd}} \mathbf{C}_m) \quad \text{in } \Omega_m. \quad (38)$$

In order to solve the resulting second-order differential equation system, a suitable time integration scheme is necessary. Here we use a JWH- $\alpha$ -scheme introduced in Kadapa et al. (2017), where also details regarding advantages and implementation of this method can be found. For the time integration, the time increment  $\Delta t$  and the additional numerical parameter  $\rho_{\infty}$  are needed. By combining the method with a regular Newton–Raphson scheme, we transform the matrix system of Eq. (32) to

$$\mathbf{R}^{i+1} := \mathbf{R}^i(d_{n+\alpha_f}, v_{n+\alpha_f}, \dot{v}_{n+\alpha_m}) - \mathbf{S} \Delta \mathbf{d} \stackrel{!}{=} \mathbf{0}, \quad (39)$$

with the index denoting the iteration and the generalized tangent matrix

$$\mathbf{S} = \frac{\alpha_m^2}{\alpha_f \gamma_a^2 \Delta t^2} \mathbf{M} + \frac{\alpha_m}{\gamma_a \Delta t} \mathbf{C} + \alpha_f \mathbf{K}, \quad (40)$$

which is the Jacobian of the system. Here  $\Delta \mathbf{d}$  is the increment of the solution vector and  $\alpha_f$ ,  $\alpha_m$  and  $\gamma_a$  are numerical

parameters depending on  $\rho_\infty$  (Kadapa et al. 2017). The residual  $\mathbf{R}^i(d_{n+\alpha_j}, v_{n+\alpha_j}, \dot{v}_{n+\alpha_m})$  is calculated from either initial conditions for the first iteration of the first time step or else from the previous increment (Kadapa et al. 2017). The resulting tangent matrix  $\mathbf{S}$  is neither symmetric nor positive definite, limiting the choices for a suitable solver of the linear system.

### 3.2 Transition between the scales

To connect the macro- and microscale in FE<sup>2</sup>, it is important to discuss the transition between the scales. The Hill-Mandel conditions (Hill 1963, 1972; Schröder 2009; Schröder et al. 2016; Labusch et al. 2019; Karimi et al. 2019) have to be fulfilled, guaranteeing energy conservation during the scale transition. Thus, the virtual work on the macroscale has to be equal to the virtual work on the microscale:

$$\begin{aligned} \bar{\boldsymbol{\sigma}} \cdot \delta \bar{\boldsymbol{\varepsilon}} &= \frac{1}{\Omega} \int_{\Omega} \boldsymbol{\sigma} \cdot \delta \boldsymbol{\varepsilon} \, dV, & \bar{\mathbf{D}} \cdot \delta \bar{\mathbf{E}} &= \frac{1}{\Omega} \int_{\Omega} \mathbf{D} \cdot \delta \mathbf{E} \, dV, \\ \bar{\mathbf{B}} \cdot \delta \bar{\mathbf{H}} &= \frac{1}{\Omega} \int_{\Omega} \mathbf{B} \cdot \delta \mathbf{H} \, dV. \end{aligned} \tag{41}$$

For the macro-to-micro-transition, these conditions can be fulfilled by three different types of boundary conditions on the microscale: Dirichlet, Neumann and periodic boundary conditions (Ilic et al. 2010; Schröder 2000; Schröder and Hackl 2013). Here we chose periodic boundary conditions, as they are the only type of boundary condition, where the results on the microscale are independent from the relative geometry of the RVE (Schröder 2000; Schröder and Hackl 2013). Additionally, as the RVE is periodic in space, this type of boundary condition is the most suitable. In the program, the periodic boundary conditions were applied by fixing all degrees of freedom at all corner nodes, preventing rigid body motions, and linking all degrees of freedom at opposite faces of the RVE, ensuring the periodicity. The micro-state variables consist then of two parts: a term resulting from the microscopic main variables (denoted by  $\tilde{\cdot}$ ), whose fluctuations are calculated, and a term contributed by the macroscale:

$$\begin{aligned} \boldsymbol{\varepsilon} &= \tilde{\boldsymbol{\varepsilon}}(\mathbf{y}) + \bar{\boldsymbol{\varepsilon}}(\mathbf{x}), & \mathbf{E} &= \tilde{\mathbf{E}}(\mathbf{y}) + \bar{\mathbf{E}}(\mathbf{x}), \\ \mathbf{B} &= \tilde{\mathbf{B}}(\mathbf{y}) + \bar{\mathbf{B}}(\mathbf{x}). \end{aligned} \tag{42}$$

This way, we calculate the flux variables on the microscale. For the micro-to-macro transition, the volume average of these flux quantities is sent back to the macroscale:

$$\begin{aligned} \bar{\boldsymbol{\sigma}}(\mathbf{x}) &= \frac{1}{\Omega} \int_{\Omega} \boldsymbol{\sigma}(\mathbf{y}) \, dV, & \bar{\mathbf{D}}(\mathbf{x}) &= \frac{1}{\Omega} \int_{\Omega} \mathbf{D}(\mathbf{y}) \, dV, \\ \dot{\bar{\mathbf{D}}}(\mathbf{x}) &= \frac{1}{\Omega} \int_{\Omega} \dot{\mathbf{D}}(\mathbf{y}) \, dV, & \bar{\mathbf{H}}(\mathbf{x}) &= \frac{1}{\Omega} \int_{\Omega} \mathbf{H}(\mathbf{y}) \, dV, \\ \bar{\mathbf{J}}(\mathbf{x}) &= \frac{1}{\Omega} \int_{\Omega} \mathbf{J}(\mathbf{y}) \, dV. \end{aligned} \tag{43}$$

In this model, energy dissipation is considered in two ways. For the electric current  $\mathbf{J}$ , the average is calculated and included in the scale transition, resulting in no energy loss during the scale transition. For the inelastic strain  $\boldsymbol{\varepsilon}^i$ , the complete state in every point and for every RVE is saved. Thus, the dissipation occurs only on the microscale and the energy conservation is fulfilled, as the virtual work sent to the microscale is equal to the virtual work sent back added to the energy dissipation on the microscale. With the flux variables available on the macroscale, it is now possible to obtain the macro-residual for the Newton–Raphson method and the calculation of consistent macro-tangent moduli remains, which are needed for the iteration. The definitions of those moduli read

$$\begin{aligned} \bar{\mathbb{C}} &:= \frac{\partial \bar{\boldsymbol{\sigma}}}{\partial \bar{\boldsymbol{\varepsilon}}}, & \bar{\boldsymbol{\xi}} &:= \frac{\partial \bar{\mathbf{D}}}{\partial \bar{\mathbf{E}}}, \\ \bar{\mathbf{e}} &:= \frac{\partial \bar{\mathbf{D}}}{\partial \bar{\boldsymbol{\varepsilon}}}, & \bar{\boldsymbol{\mu}}^{-1} &:= \frac{\partial \bar{\mathbf{H}}}{\partial \bar{\mathbf{B}}}, \\ \bar{\boldsymbol{\kappa}} &:= \frac{\partial \bar{\mathbf{J}}}{\partial \bar{\mathbf{E}}}. \end{aligned} \tag{44}$$

The calculation can be done by applying a small numerical perturbation  $\Delta_{\text{tol}} = 10^{-8}$  to each entry of the corresponding state variable

$$\begin{aligned} \bar{\boldsymbol{\varepsilon}}^{p_i} &= \bar{\boldsymbol{\varepsilon}} + \Delta_{\text{tol}} e_i, & \bar{\mathbf{E}}^{p_i} &= \bar{\mathbf{E}} + \Delta_{\text{tol}} e_i, \\ \bar{\mathbf{B}}^{p_i} &= \bar{\mathbf{B}} + \Delta_{\text{tol}} e_i, \end{aligned} \tag{45}$$

with the  $i$ -th unit vector  $e_i$ , and then calculating each entry of the macroscopic tangent tensors by evaluating the perturbed fluxes  $\bar{\boldsymbol{\sigma}}^{p_i}, \bar{\mathbf{D}}^{p_i}, \bar{\mathbf{H}}^{p_i}, \bar{\mathbf{J}}^{p_i}$  by means of the RVE as

$$\begin{aligned} \bar{\mathbb{C}}_{ji} &= \frac{\bar{\boldsymbol{\sigma}}_j^{p_i} - \bar{\boldsymbol{\sigma}}_j}{\bar{\boldsymbol{\varepsilon}}_j^{p_i} - \bar{\boldsymbol{\varepsilon}}_j}, & \bar{\boldsymbol{\xi}}_{ji} &= \frac{\bar{D}_j^{p_i} - \bar{D}_j}{\bar{E}_j^{p_i} - \bar{E}_j}, \\ \bar{e}_{ji} &= \frac{\bar{D}_j^{p_i} - \bar{D}_j}{\bar{\boldsymbol{\varepsilon}}_j^{p_i} - \bar{\boldsymbol{\varepsilon}}_j}, & \bar{\boldsymbol{\mu}}_{ji}^{-1} &= \frac{\bar{H}_j^{p_i} - \bar{H}_j}{\bar{B}_j^{p_i} - \bar{B}_j}, \\ \bar{\boldsymbol{\kappa}}_{ji} &= \frac{\bar{J}_j^{p_i} - \bar{J}_j}{\bar{E}_j^{p_i} - \bar{E}_j}. \end{aligned} \tag{46}$$



Since for our model the same RVE is used everywhere and the nonlinearity from the inelastic strain is very small, this calculation has to be done only once for all RVEs and all time steps, making this approach very efficient. Together with the calculated macrostate variables, this allows to solve the macroscopic FE problem.

### 3.3 Implementation

For the simulations, we implemented a computer program in the language JULIA (The julia programming language 2021), using mainly the packages JUAFFEM (Carlsson and Ekre 2021) and COHERENTSTRUCTURES (de Diego et al. 2021). As the microscale calculations are not dependent on each other, we have parallelized the macroscale element routine, increasing the speed of the computations drastically. As the inelastic strain  $\epsilon^i$  is only present in the microscale, we used HDF5 files to store the complete state of the inelastic strain for every RVE for the previous and current time step. Thus, for the inelastic strain evolution no information is lost. In order to solve the linear systems, we used the BiCGStab(l) method of the package KRYLOVMETHODS (Krylovmethods 2021), as it is stable, fast even without preconditioning the problem and can be used for any matrix type. Regarding the structure of the program, Fig. 3 shows the procedure.

## 4 Simulation results

### 4.1 Parameters and material tensors

In this subsection, we discuss the numerical and material parameters employed. Unless explicitly stated otherwise, the parameters from this subsection are used in all simulations. Regarding the numerical parameters, we use the same parameters for both scales. The time integration parameter is  $\rho_\infty = 0.5$ , the Newton–Raphson tolerance is  $\text{tol}_N = 1 \cdot 10^{-8}$  and the gauge penalty parameter is  $\gamma = 1.0 \text{ s}^2 \text{ A}^2/(\text{kg m})$ . The load and numerical time step increment depending on the model are shown in Table 1.

The used default material parameters are shown in Table 2. Young’s modulus and Poisson’s ratio for both phases can be found in Steeb (2010). The piezoelectric coefficient can be found in Fukada and Yasuda (1957). For the magnetic properties, bone is considered as a nonmagnetizable material, thus having the same permeability as the vacuum (Güzelsu and Saha 1981). All other parameters are of rather academical nature and influence the results only marginally. The resulting material tensors read

$$\mathbb{C} = \frac{E}{(1 + \nu)(1 - 2\nu)} \cdot \begin{pmatrix} 1 - \nu & \nu & \nu & 0 & 0 & 0 \\ \nu & 1 - \nu & \nu & 0 & 0 & 0 \\ \nu & \nu & 1 - \nu & 0 & 0 & 0 \\ 0 & 0 & 0 & \frac{1-2\nu}{2} & 0 & 0 \\ 0 & 0 & 0 & 0 & \frac{1-2\nu}{2} & 0 \\ 0 & 0 & 0 & 0 & 0 & \frac{1-2\nu}{2} \end{pmatrix}, \tag{47}$$

$$\begin{aligned} \xi &= \begin{pmatrix} \xi_1 & 0 & 0 \\ 0 & \xi_1 & 0 \\ 0 & 0 & \xi_1 \end{pmatrix}, & \mathbf{e} &= \begin{pmatrix} 0 & 0 & 0 & 0 & e_{15} & 0 \\ 0 & 0 & 0 & 0 & 0 & -e_{15} \\ 0 & 0 & 0 & 0 & 0 & 0 \end{pmatrix}, \\ \mu^{-1} &= \begin{pmatrix} \mu_c^{-1} & 0 & 0 \\ 0 & \mu_c^{-1} & 0 \\ 0 & 0 & \mu_c^{-1} \end{pmatrix}, & \boldsymbol{\kappa} &= \begin{pmatrix} \kappa_1 & 0 & 0 \\ 0 & \kappa_1 & 0 \\ 0 & 0 & \kappa_1 \end{pmatrix}. \end{aligned} \tag{48}$$

We assume linear isotropic material everywhere, excluding the piezoelectric tensor which is preferential in the  $z$ -axis due to the longitudinal orientation of the collagen fibers. It should be noted, that due to the form of the piezoelectric tensor, the material model as a whole is non-isotropic.

For the generation of the meshes, we used the program GMSH (Geuzaine and Remacle 2021). We did the visualization of the results with PARAVIEW (Paraview 2021) and JULIA (The julia programming language 2021).

### 4.2 Microscale model

In this subsection, we restrict ourselves to microscale simulations. In order to compare periodic RVEs for different stages of osteoporosis, we introduce the lengths parameters  $a$  and  $b$  (Fig. 4), which allow us to control the volume fractions of the phases. By using this convention, the total volume of the RVE is  $V_{\text{RVE}} = (2a + b)^3$ . We only use RVEs with the same total volume of  $V_{\text{RVE}} = 1 \text{ mm}^3$ , which is a suitable size for the microscale calculations (Ilic et al. 2010), making it easy to compare different RVEs. Thus, the choice of  $a$  and  $b$  is restricted by  $2a + b = 1 \text{ mm}$ . The volume fraction of cortical bone for our RVE is  $\rho_b = (6ab^2 + b^3)/(2a + b)^3$ .

In our first example, we use a healthy bone RVE with the parameters  $a = 0.32 \text{ mm}$  and  $b = 0.36 \text{ mm}$ , resulting in  $\rho_b = 29.5\%$ . We compare different mesh resolutions. The first RVE consists of two elements in each phase block, resulting in six elements for each spatial direction. The second RVE consists of four elements in each block, resulting in

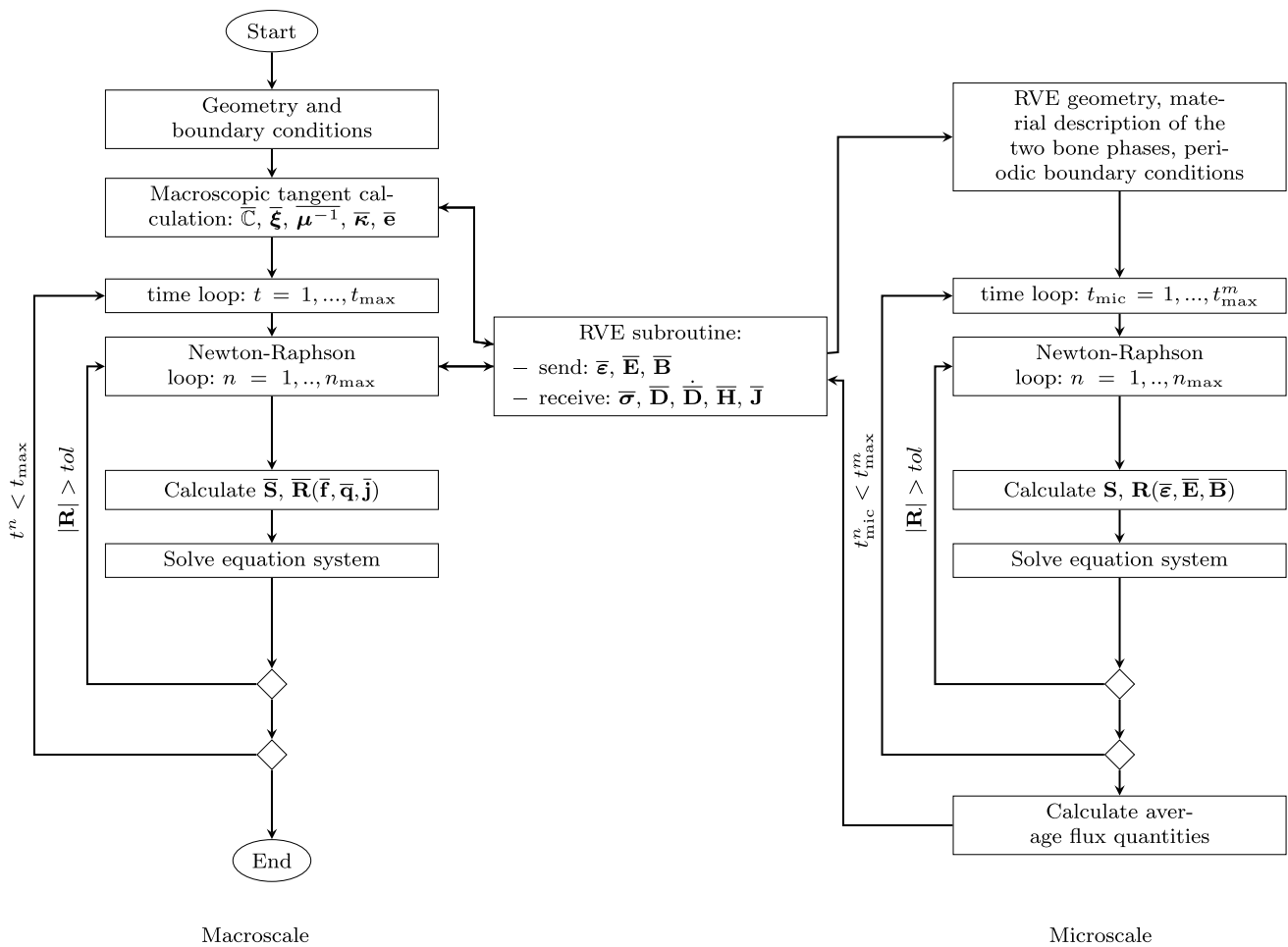


Fig. 3 Program flow of the multiscale simulations

Table 1 Load and numerical time step increment for the different models

| Model           | Load                                    | Time step                      |
|-----------------|---|--------------------------------|
| Microscale cube | $\bar{\epsilon}_{yz} = 1 \cdot 10^{-5}$ | $\Delta_t = 1 \cdot 10^{-3}$ s |
| Cylinder        | $u_{\max} = 2 \cdot 10^{-6}$ m          | $\Delta_t = 1 \cdot 10^{-2}$ s |
| Femur bone      | $u_{\max} = 2 \cdot 10^{-6}$ m          | $\Delta_t = 1 \cdot 10^{-2}$ s |

twelve elements for each spatial direction. Here, all degrees of freedom for all corner nodes are restricted to zero and all opposite nodes are linked, to guarantee periodicity. Figure 5 shows the results of the simulations.

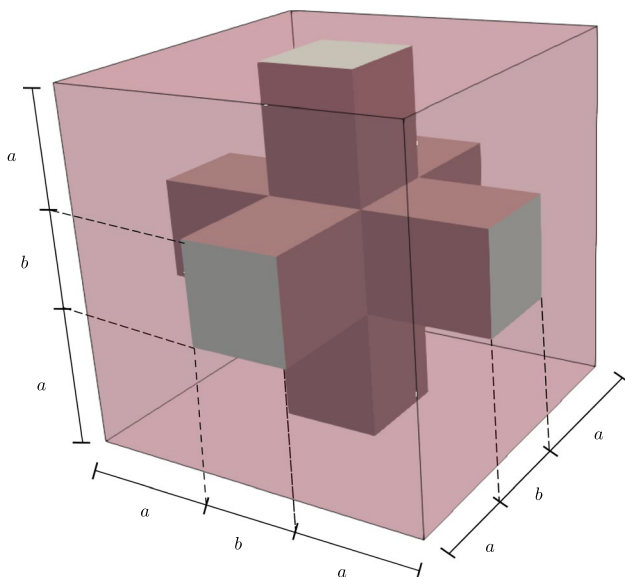
Both simulations show quadratic convergence behavior and periodic results. For all quantities, the results between the two different used meshes look nearly identical

Table 2 Default material parameters

| Material parameter        |            | Cortical bone         |                   | Bone marrow           |                   |
|---------------------------|------------|-----------------------|-------------------|-----------------------|-------------------|
| Young's modulus           | $E$        | 22.0                  | GPa               | 2.0                   | GPa               |
| Poisson's ratio           | $\nu$      | 0.32                  | –                 | 0.3                   | –                 |
| Permittivity              | $\xi_1$    | $8.85 \cdot 10^{-12}$ | F/m               | $8.85 \cdot 10^{-12}$ | F/m               |
| Permeability              | $\mu_c$    | $1.257 \cdot 10^{-6}$ | H/m               | $1.257 \cdot 10^{-6}$ | H/m               |
| Piezoelectric coefficient | $e_{15}$   | $3.0 \cdot 10^{-3}$   | As/m <sup>2</sup> | 0                     | As/m <sup>2</sup> |
| Electric conductivity     | $\kappa_1$ | 0                     | S/m               | $1.0 \cdot 10^4$      | S/m               |
| Viscosity parameter       | $\mu_v$    | 0                     | s/GPa             | $0.5 \cdot \Delta_t$  | s/GPa             |

confirming mesh independence of the results. This is not only fulfilled on the surface of the model, but also in the inner parts, as the slice (top right) shows. It should be noted that since the FE<sup>2</sup> method uses volume averaging, the coarse mesh with only six elements in each spatial direction is sufficient enough to create accurate results for the multiscale method and is mostly used in the remaining examples of this paper.

The calculation of the magnetic field strength is susceptible for numerical errors. These errors can occur, when there are sharp edges in the mesh or between the phase transitions, which can amplify the results. To investigate this issue, we constructed smoother RVEs by using tetrahedron elements and different mesh resolutions. Figure 6 shows the used meshes. We found that despite the smoother approach, the numerical results of the RVEs with tetrahedron elements are much worse compared to the RVEs with hexahedron elements, showing worse convergence behavior and overestimating the magnetic field strength. One reason for this result could be that through the mesh refinement, many additional corners are introduced, which in total amplify the magnetic field strength more than a low number of very sharp corners. Moreover, smaller element size leads to amplified singularities of the corresponding fields at corners, which otherwise are regularized by the employed shape functions. Similarly, Fig. 5 shows an increase in the magnetic field strength for the finer mesh resolution of the RVEs with hexahedron elements. In conclusion, the coarse RVE with hexahedron elements shows the best numerical performance despite the low mesh resolution and the included sharp edges.



**Fig. 4** Periodic RVE with cortical bone phase (gray) and bone marrow phase (transparent red) and lengths parameters

To compare the model behavior for different stages of osteoporosis, we created RVEs with different volume fractions of cortical bone. Table 3 shows the choice of the lengths parameters and the resulting volume fractions. The macroscopic mechanical stiffness tensor  $\bar{\mathbf{C}} := \frac{\partial \bar{\sigma}}{\partial \bar{\epsilon}}$  was now evaluated for all RVEs by applying a small numerical perturbation as discussed in Sect. 3.2. We then calculate the effective Young’s modulus as

$$E_{\text{eff}} = \frac{\bar{C}_{44}(3\bar{C}_{12} + 2\bar{C}_{44})}{(\bar{C}_{12} + \bar{C}_{44})} \tag{49}$$

Figure 7 shows a plot of the macroscopic Young’s modulus against the volume fraction of cortical bone. Here, we observe a drastical reduction of the macroscopic Young’s modulus with decreasing cortical bone fraction. Compared to a healthy bone ( $\rho_b = 29.5\%$ ), the effective Young’s modulus of the degenerated bone ( $\rho_b = 5.3\%$ ) decreases to 57% (from 3.89 GPa to 2.32 GPa). Similar results can be found in Ilic et al. (2010).

### 4.3 Cylinder model

In this section, we show results for a cylinder model, which has a length of 30 cm and a diameter of  $2 r_o = 3$  cm. The mesh and the displacement boundary conditions are shown in Fig. 8. The mesh consists of 1767 nodes and 1440 hexahedral elements. The left and right face is fixed, resulting in the boundary conditions  $\mathbf{u} = \mathbf{0}$  on the faces. Additionally, in the inner part of the left face ( $r < r_i = 0.75$  cm) depicted in Fig. 9, the cylinder is assumed to be grounded, resulting in  $\varphi = 0$  and  $\mathbf{A} = \mathbf{0}$ . We apply a time-dependent mechanical displacement in x-direction  $u_x = u_{\text{max}} \cdot a(t)$  to the middle part of the cylinder and calculate 100 time steps. Figure 10 shows the amplitude of the displacement function  $a$  versus the time  $t$ .

First, we examine the simulation results for the healthy bone (RVE 6,  $\rho_b = 29.5\%$ ). Here, we observe quadratic convergence behavior for the macroscale as well. Figures 11 and 12 show the magnitude of the average electric displacement field  $\mathbf{D}$  and the magnitude of the average magnetic field strength  $\mathbf{H}$ , respectively, plotted against time  $t$ . The history of the average electric displacement field mimics

**Table 3** Lengths parameter of the different RVEs

| no. | $a$ [mm] | $b$ [mm] | $\rho_b$ |
|-----|----------|----------|----------|
| 1   | 0.43     | 0.14     | 5.3%     |
| 2   | 0.40     | 0.20     | 10.4%    |
| 3   | 0.38     | 0.24     | 14.5%    |
| 4   | 0.36     | 0.28     | 19.1%    |
| 5   | 0.34     | 0.32     | 24.2%    |
| 6   | 0.32     | 0.36     | 29.5%    |

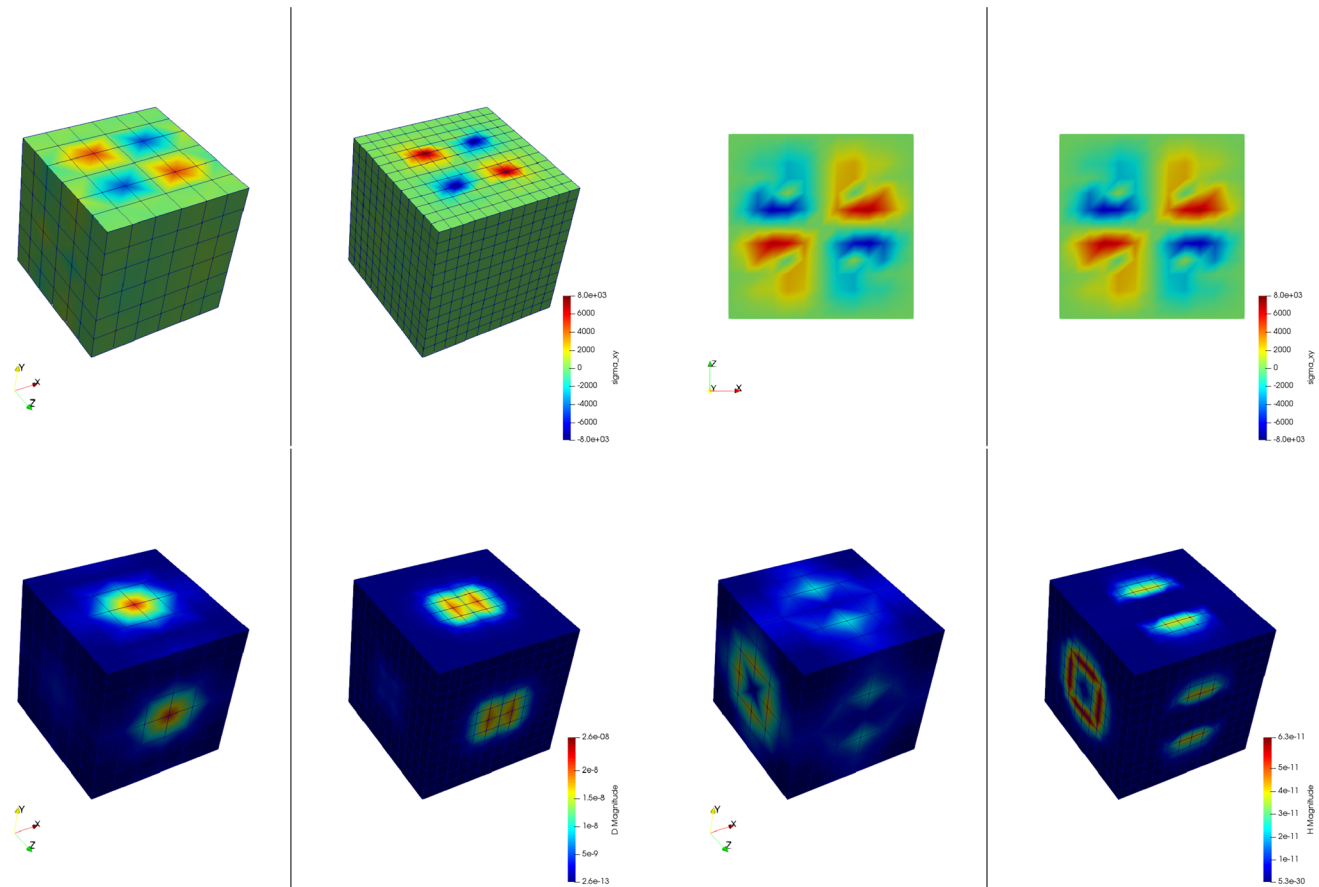


**Fig. 5** Microscale simulation results of a coarse and fine mesh (left and right respectively) for all flux quantities. Top left: mechanical stress  $\sigma_{xy}$  [GPa], top right: mechanical stress  $\sigma_{xy}$  [GPa] in the  $xz$ -plane

with  $y = 0$ , bottom left: magnitude of the electric displacement field  $\mathbf{D}$  [As/m<sup>2</sup>], bottom right: magnitude of the magnetic field strength  $\mathbf{H}$  [A/m]

the displacement boundary condition. Thus, the electric displacement field is caused mainly by the piezoelectric effect of the cortical bone material phase. In contrast, the magnitude of the average magnetic field strength increases until time  $t = 50$ , where the maximum is reached. Then, the magnitude decreases again and at the end of the simulation, only a small amount of the magnetic field is present. We conclude, that the magnetic field is caused mainly by the time change of the electric displacement field as described by the Maxwell equations.

To compare the different stages of osteoporosis, we use different RVEs (Table 3). The simulation results are shown in Figs. 13, 14, 15, 16. Here, the number of the specific RVE increases from top to bottom.

As an additional example for the cylinder model, we performed a parameter study for the electric conductivity parameter  $\kappa_1$ , aiming to understand the interaction between the time derivative of the electric displacement field and the electric current density in the Maxwell equation. Figures 17 and 18 show the results for RVE 1 and  $\kappa_1 \in \{1 \cdot 10^2 \text{ S/m}, 1 \cdot 10^4 \text{ S/m}, 1 \cdot 10^6 \text{ S/m}\}$ .

For all quantities, we observe an increase for RVEs with higher volume fractions of cortical bone. Additionally, the difference between the RVEs is greater, the lower the volume fraction of cortical bone is. While the difference is barely noticeable between RVE 5 and 6, the change of all quantities excluding the stress is distinct between RVEs 1 and 2. Qualitatively, we notice similar results between the different RVEs.

Regarding the parameter study of the electric conductivity, we observe nearly identical results for the magnetic field strength  $\mathbf{H}$  for the first two choices of  $\kappa_1$ , but a significant increase for  $\kappa_1 = 1 \cdot 10^6 \text{ S/m}$ . Similarly the electric current density  $\mathbf{J}$  increases proportionally to the increase of the material parameter. Thus, for the first two choices of  $\kappa_1$ , nearly no magnetic field and electric current is visible.

Real bones can be highly anisotropic. To investigate possible effects on the simulation results, we constructed an anisotropic RVE, which is longer (Fig. 19) and therefore also is divided into ten instead of six elements in  $z$ -direction. We used the parameters  $a = 0.29 \text{ mm}$  and  $b = 0.42 \text{ mm}$ ,

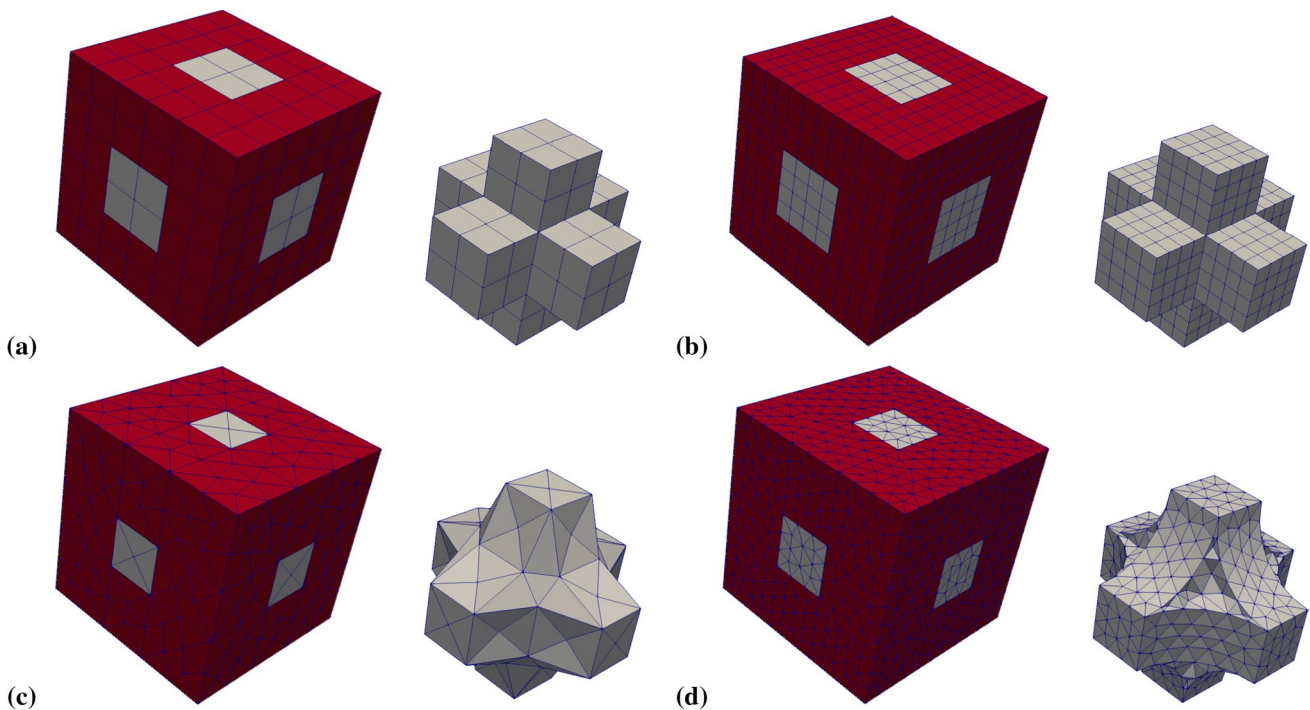


**Fig. 6** Used meshes for the complete RVE (left) and only the cortical bone phase (right). **a** coarse hexahedron mesh, **b** fine hexahedron mesh, **c** coarse tetrahedron mesh, **d** fine tetrahedron mesh

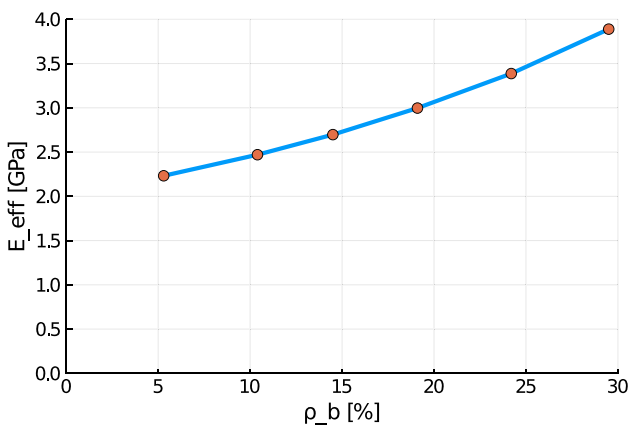


**Fig. 7** Effective Young's modulus  $E_{eff}$  against cortical bone volume fraction  $\rho_b$  for different RVEs

resulting in a total RVE volume  $V_{RVE} = 1.58 \text{ mm}^3$  and a volume fraction of cortical bone  $\rho_b = 30.6\%$ . We compare our calculations to the isotropic RVE 6, which has a similar volume fraction of cortical bone. The results are shown in Figs. 20 and 21. We obtain similar results for both RVE geometries. The calculated stress is slightly higher for the anisotropic RVE. The magnetic field strength is about 15% increased for the anisotropic RVE compared to the cubic RVE.

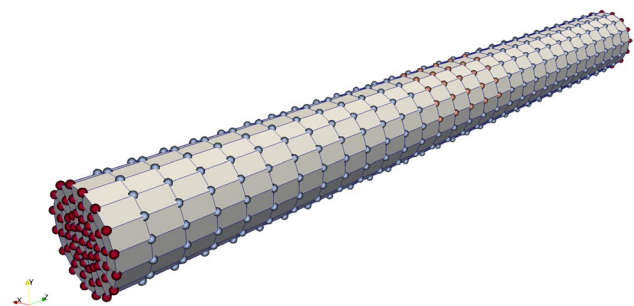


**Fig. 8** Cylinder mesh and displacement boundary conditions (red: all directions restricted, orange: only the x-direction restricted, blue-gray: no directions restricted)

#### 4.4 True to scale bone model

We examine a true to scale model of a human femur bone from Lifescience (2021) and slightly modify it by using the software BLENDER (Blender 2021), improving the mesh. Again the model has a length of about 30 cm. The mesh and the displacement boundary conditions are shown in Fig. 22. The mesh consists of 1660 nodes and 4944 tetrahedral elements. The grounded nodes are shown in Fig. 23. Again, we apply the mechanical displacement depicted in Fig. 10 to the middle section and calculate 100 time steps. To compare



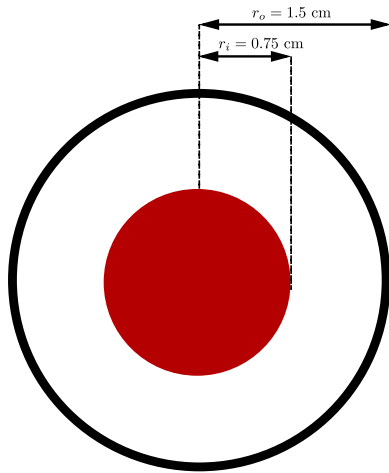


**Fig. 9** Cylinder front in the  $xy$ -plane for  $z = 0$  with grounded nodes in red

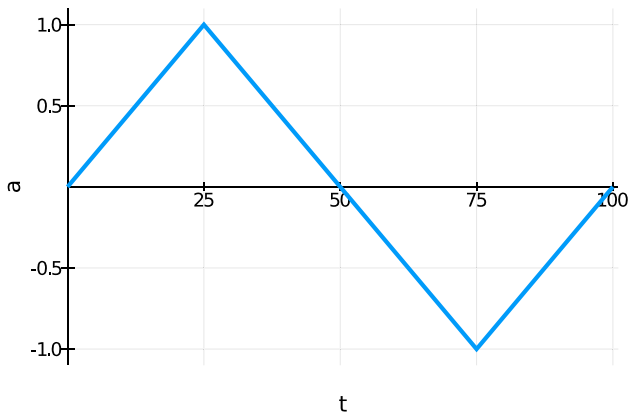


**Fig. 10** Amplitude of the displacement function  $a$  against the time step  $t$

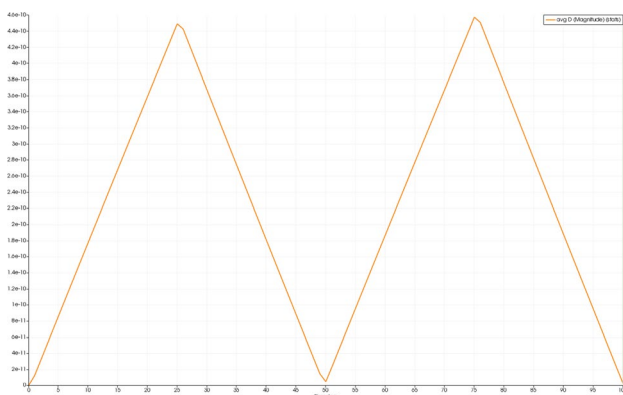


**Fig. 11** Magnitude of the average electric displacement field  $\mathbf{D}$  [ $\text{As}/\text{m}^2$ ], plotted against the time  $t$

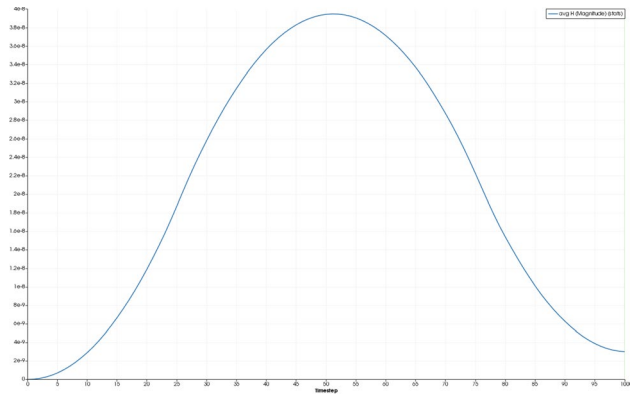


**Fig. 12** Magnitude of the average magnetic field strength  $\mathbf{H}$  [ $\text{A}/\text{m}$ ], plotted against the time  $t$

different stages of osteoporosis, we use again different RVEs (Table 3). Figures 24, 25, 26, 27, 28, 29 show the results.

Again, the simulations show qualitatively similar results, but a significant increase for all quantities the higher the cortical bone volume fraction is. Compared to the cylinder model, we receive slightly higher numerical values, which lie in the same magnitudes. The reason for this is most likely the used mesh, which has sharper corners due to the geometry of bone. Additionally, tetrahedron elements usually perform worse compared to hexahedron elements. The difference between the RVEs is smaller the higher the volume fraction of cortical bone is. Thus, both the functionality of the bone and the results of the sonography are only slightly affected at earlier stages of osteoporosis, but significantly at later ones. This confirms the disease as being often imperceptible for many subjects at earlier stages. This is especially important regarding the magnetic field strength  $\mathbf{H}$ , as it is the quantity measured at sonography-aided early detection. To further examine the results, we calculate the average and maximum magnetic field strength  $\mathbf{H}$  at time step  $t = 50$  for the different RVEs. The results are shown in Figs. 30 and 31.

Here, for both quantities a similar behavior can be observed. While there is nearly no reduction between the two RVEs with the highest volume fraction of cortical bone, the difference between the single RVEs increases for lower volume fractions of cortical bone. The average magnetic field strength reduces for the ill bone ( $\rho_b = 5.3\%$ ) to 36.5% compared to the healthy bone ( $\rho_b = 29.5\%$ ), from  $3.14 \cdot 10^{-7} \text{ A}/\text{m}$  to  $1.15 \cdot 10^{-7} \text{ A}/\text{m}$ . The maximum magnetic field strength for the healthy bone is  $2.711 \cdot 10^{-6} \text{ A}/\text{m}$ , while the maximum for the degenerated bone is only  $1.038 \cdot 10^{-6} \text{ A}/\text{m}$ . This equals a reduction to 38.2%. These results show the order of magnitude to be expected for the results of experimental research. For advanced stages of osteoporosis, sonography should



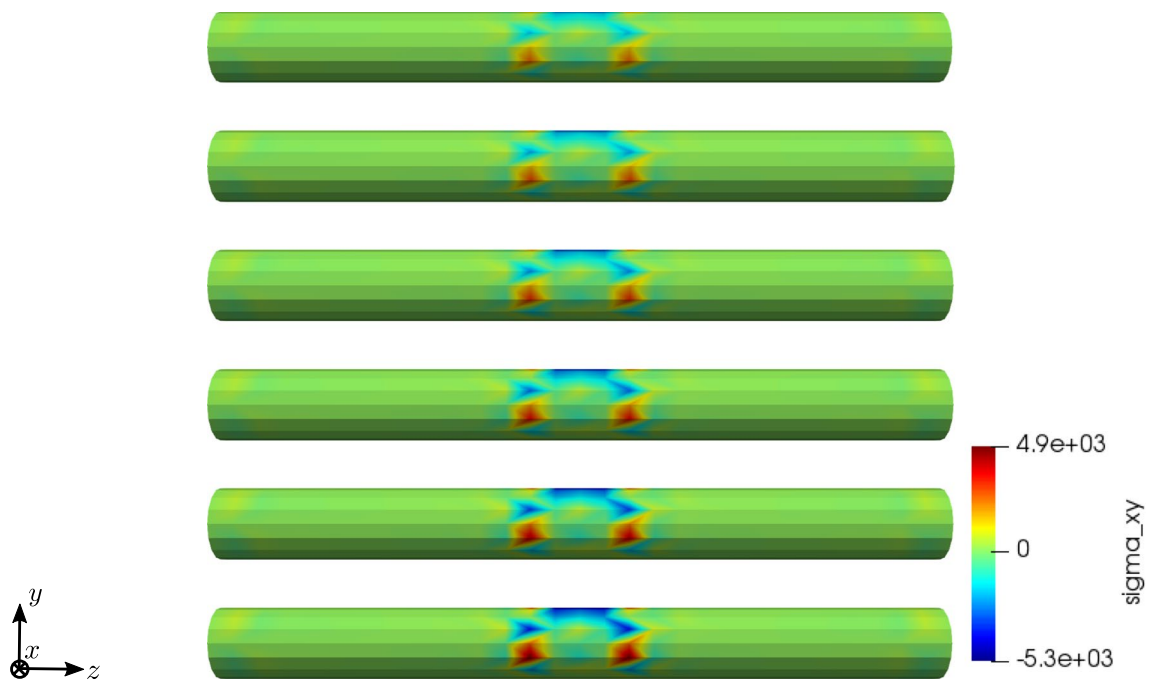


Fig. 13 Simulation results for RVE 1 (top) to 6 (bottom): stress  $\sigma_{xy}$  [GPa],  $t = 25$

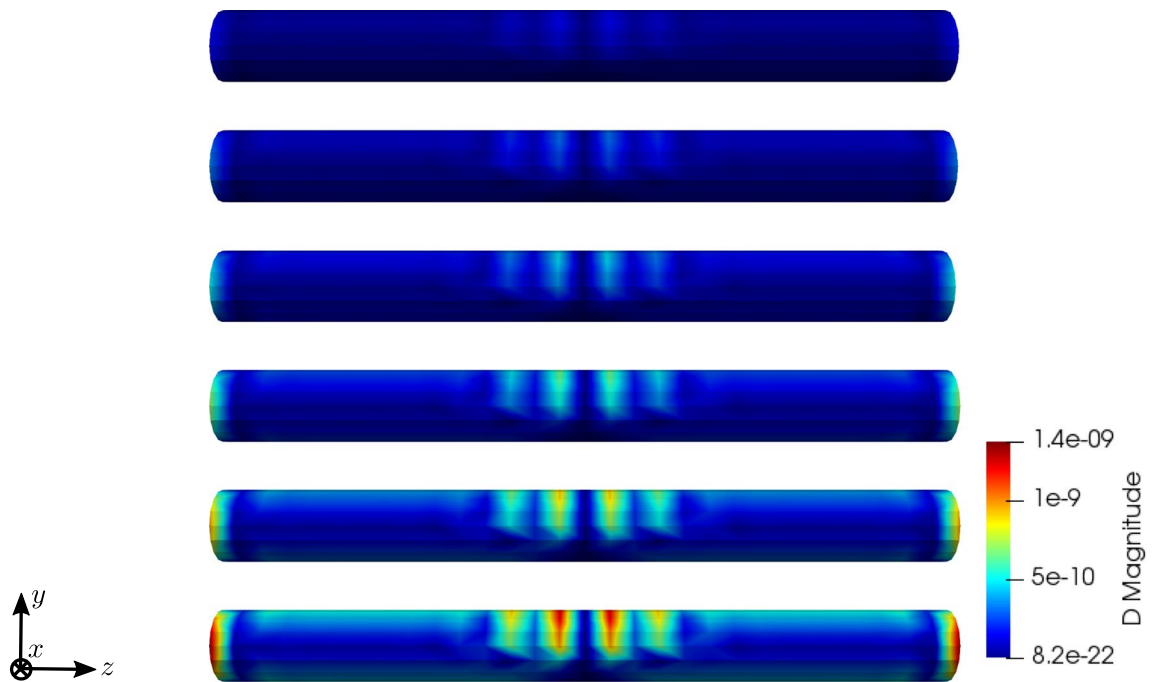
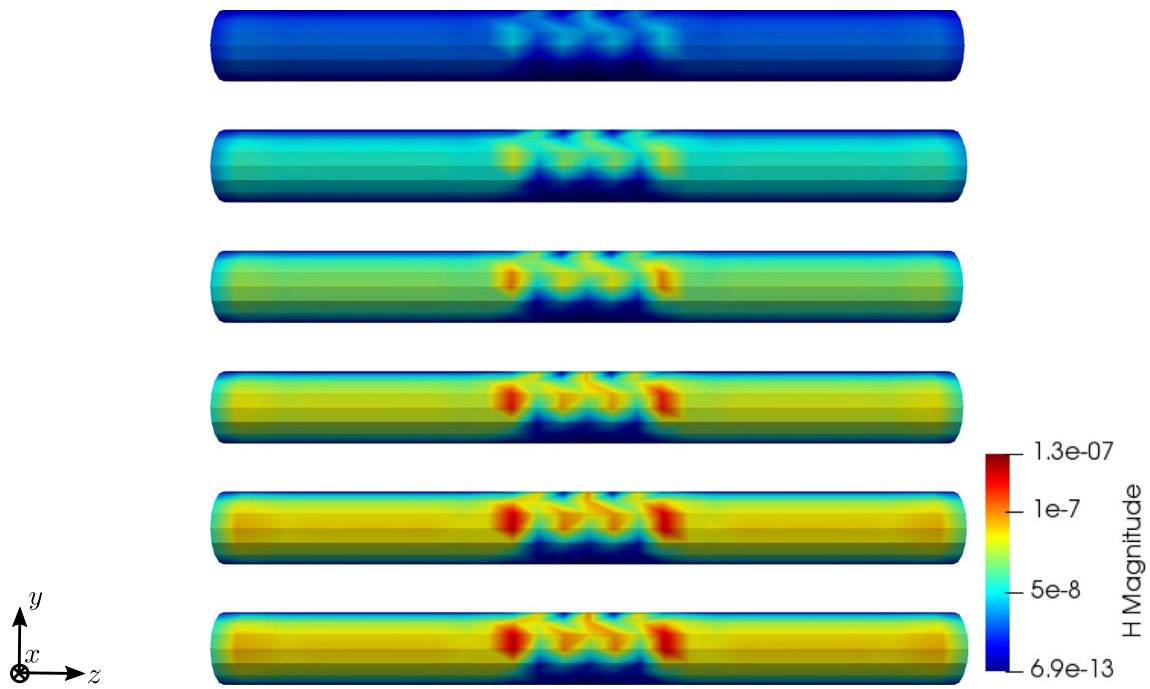
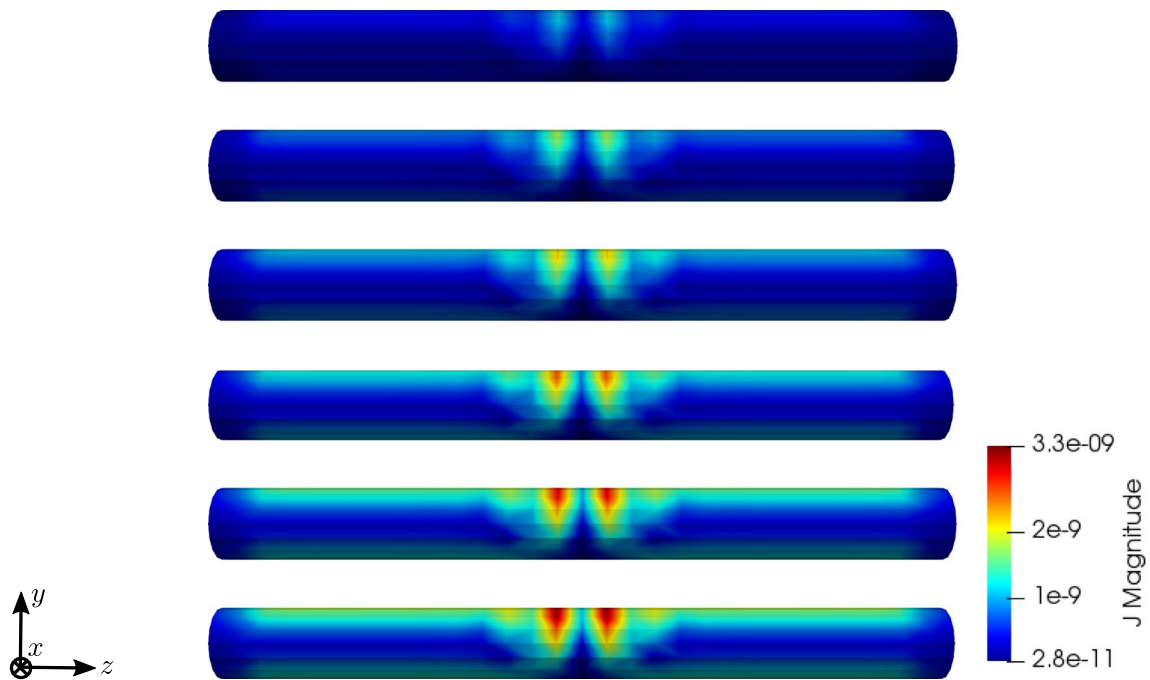


Fig. 14 Simulation results for RVE 1 (top) to 6 (bottom): magnitude of the electric displacement field  $\mathbf{D}$  [As/m<sup>2</sup>],  $t = 25$



**Fig. 15** Simulation results for RVE 1 (top) to 6 (bottom): magnitude of the magnetic field strength  $\mathbf{H}$  [A/m],  $t = 50$



**Fig. 16** Simulation results for RVE 1 (top) to 6 (bottom): magnitude of the electric current density  $\mathbf{J}$  [A/m<sup>2</sup>],  $t = 50$

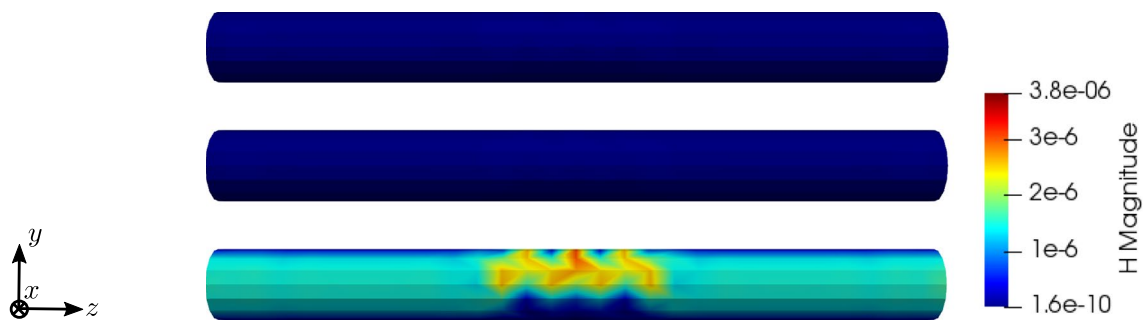


**Fig. 17** Simulation results for RVE 1 for the magnetic field strength  $\mathbf{H}$  [A/m] with  $\kappa_1 = 1 \cdot 10^2$  S/m (top),  $\kappa_1 = 1 \cdot 10^4$  S/m (in the middle) and  $\kappa_1 = 1 \cdot 10^6$  S/m (bottom),  $t = 50$



**Fig. 18** Simulation results for RVE 1 for the electric current density  $\mathbf{J}$  [A/m<sup>2</sup>] with  $\kappa_1 = 1 \cdot 10^2$  S/m (top),  $\kappa_1 = 1 \cdot 10^4$  S/m (in the middle) and  $\kappa_1 = 1 \cdot 10^6$  S/m (bottom),  $t = 50$

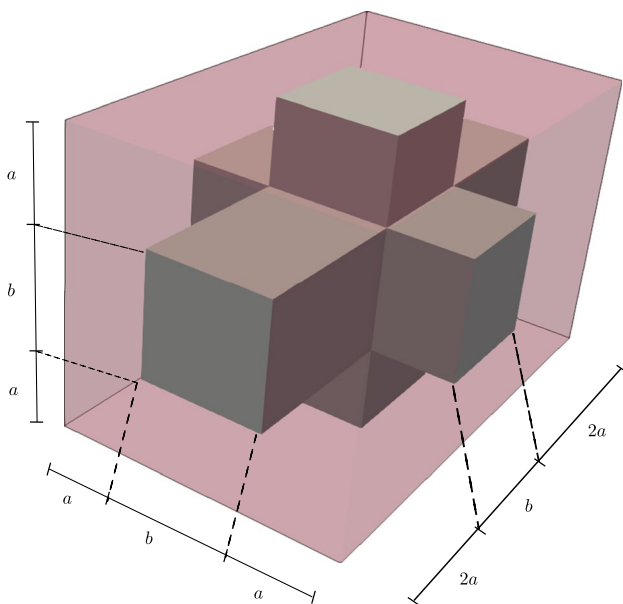


**Fig. 19** Anisotropic RVE with cortical bone phase (gray) and bone marrow phase (transparent red) and lengths parameters

measure a magnetic field strength, whose magnitude is only about one third compared to a healthy bone.

### 5 Conclusion and outlook

In this contribution, we present a fully coupled multi-scale model for cancellous bone considering mechanical, electric and magnetic effects. We model bone as a two-phase material with the cortical bone phase assumed as a piezoelectric, insulating solid and the bone marrow phase described as a viscoelastic, conducting solid. Electric and magnetic effects are coupled via the Maxwell equations. Based on energy methods in mechanics, we establish a thermodynamically consistent material model and derive the weak and strong form of the microscale boundary value problem.

In order to solve the macroscale problem, we create an RVE and apply the FEM to solve the problem numerically. For the time integration of the FEM, we use a JWH- $\alpha$ -scheme (Kadapa et al. 2017). The numerical simulations on the microscale show mesh independence and quadratic convergence. For finer mesh resolutions or smoother geometries of the phases, the model tends to overestimate the magnetic field strength. Additionally, we show that the

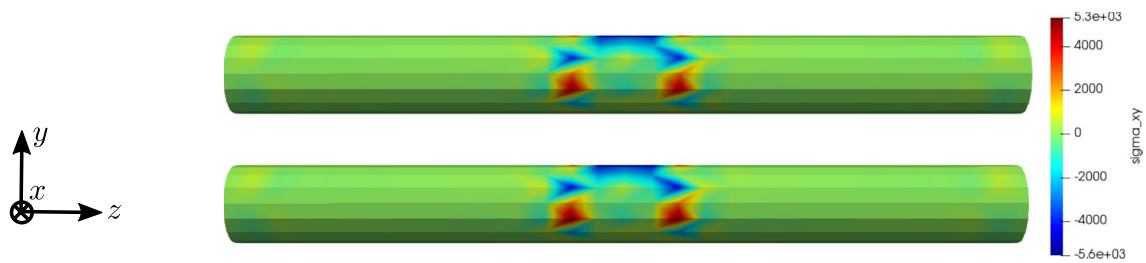


**Fig. 20** Simulation results for RVE 6 (top) and the anisotropic RVE (bottom) for the stress  $\sigma_{xy}$  [GPa],  $t = 25$

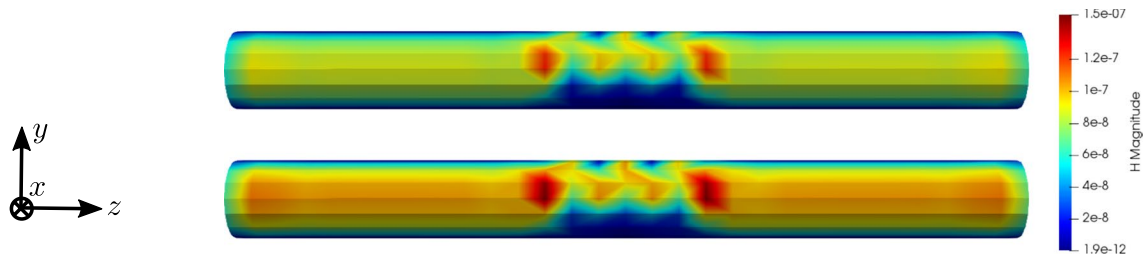


**Fig. 21** Simulation results for RVE 6 (top) and the anisotropic RVE (bottom) for the magnetic field strength  $\mathbf{H}$  [A/m],  $t = 50$

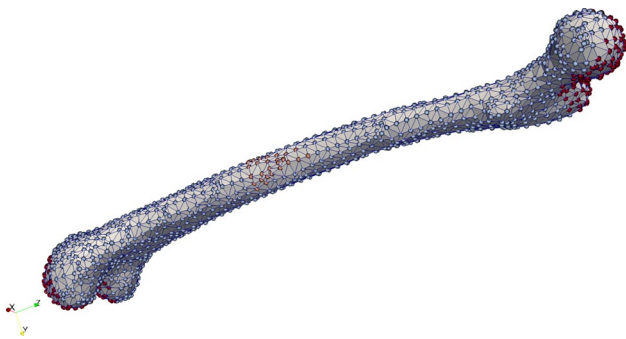


**Fig. 22** Femur bone mesh and displacement boundary conditions (red: all directions restricted, orange: only the x-direction restricted, blue-gray: no directions restricted)

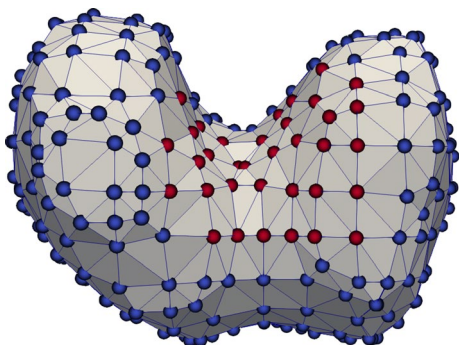


**Fig. 23** Femur bone front with grounded nodes in red

effective Young's modulus of the RVE depends strongly on the volume fraction of the different phases. Here, we find a reduction by 43% for the degenerated bone ( $\rho_b = 5.3\%$ ) compared to the healthy bone ( $\rho_b = 29.5\%$ ), achieving similar results as in Ilic et al. (2010).

For the multiscale calculations, we use  $\text{FE}^2$  and apply periodic boundary conditions and volume averaging for the transition between the scales. We apply a time-dependent displacement boundary condition. The macroscopic cylinder model again shows quadratic convergence. To compare different stages of osteoporosis with a healthy bone, we create six different RVEs with different volume fractions of cortical bone phase and run calculations for all RVEs. The simulations show a strong reduction of all quantities with decreasing volume fraction of cortical bone phase. The differences between the healthy bone RVE ( $\rho_b = 29.5\%$ ) and a slightly degenerated bone ( $\rho_b = 24.2\%$ ) are very small, while the differences in the later stages of the illness, ( $\rho_b = 10.4\%$  compared to  $\rho_b = 5.3\%$ ), increase drastically. To examine the interaction between the time derivative of the electric displacement field and the electric current density in the Maxwell equation, we perform a parameter study regarding the electric conductivity parameter  $\kappa_1$ . Here, the results show a significant increase of the electric current density and the magnetic field strength with increasing  $\kappa_1$ . To investigate the effect of anisotropy on the model, we compared our cubic RVE with an anisotropic cuboid RVE. Depending on the used RVE geometry, the results can vary slightly.

As a final example, we apply our model to a true to scale model of a human femur bone. Here, the results

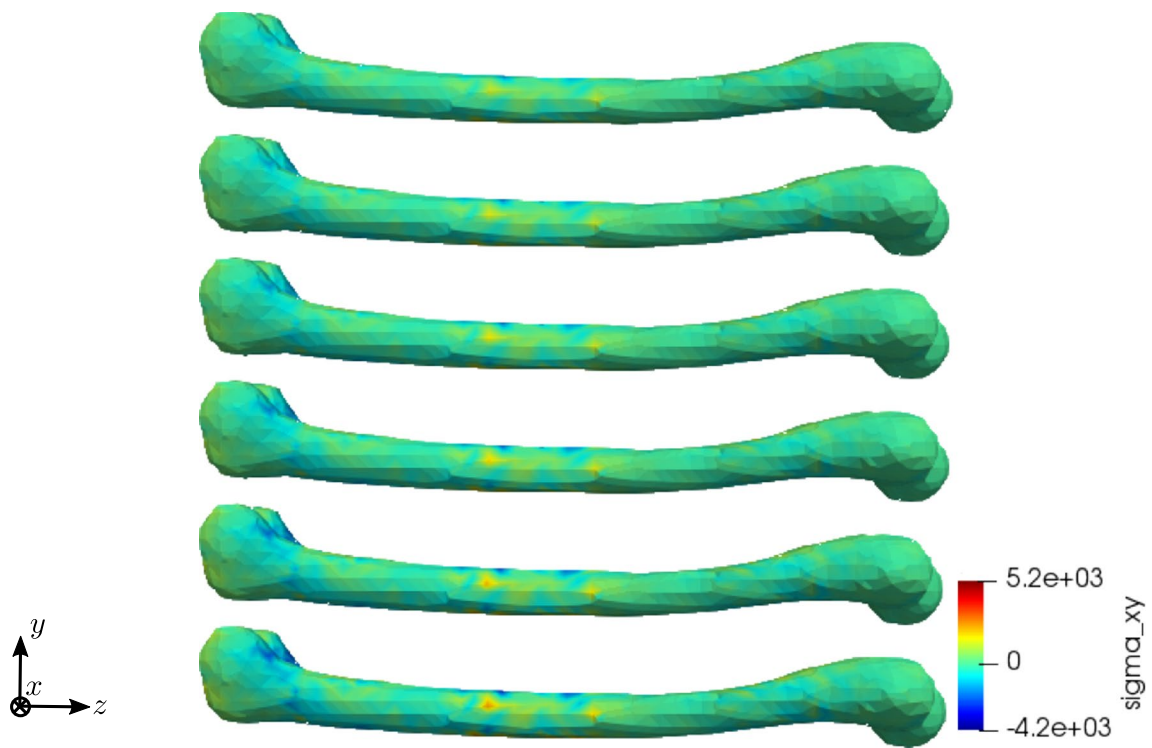


Fig. 24 Simulation results for RVE 1 (top) to 6 (bottom): stress  $\sigma_{xy}$  [GPa],  $t = 25$

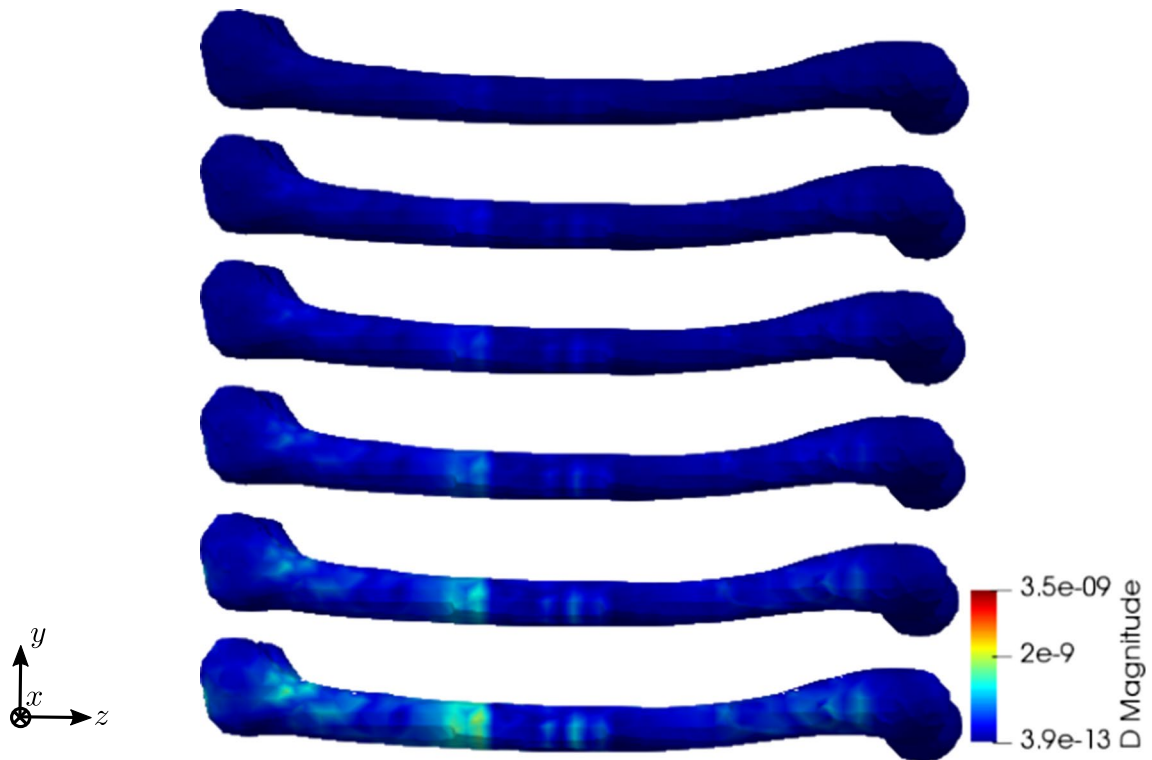


Fig. 25 Simulation results for RVE 1 (top) to 6 (bottom): magnitude of the electric displacement field  $\mathbf{D}$  [As/m<sup>2</sup>],  $t = 25$



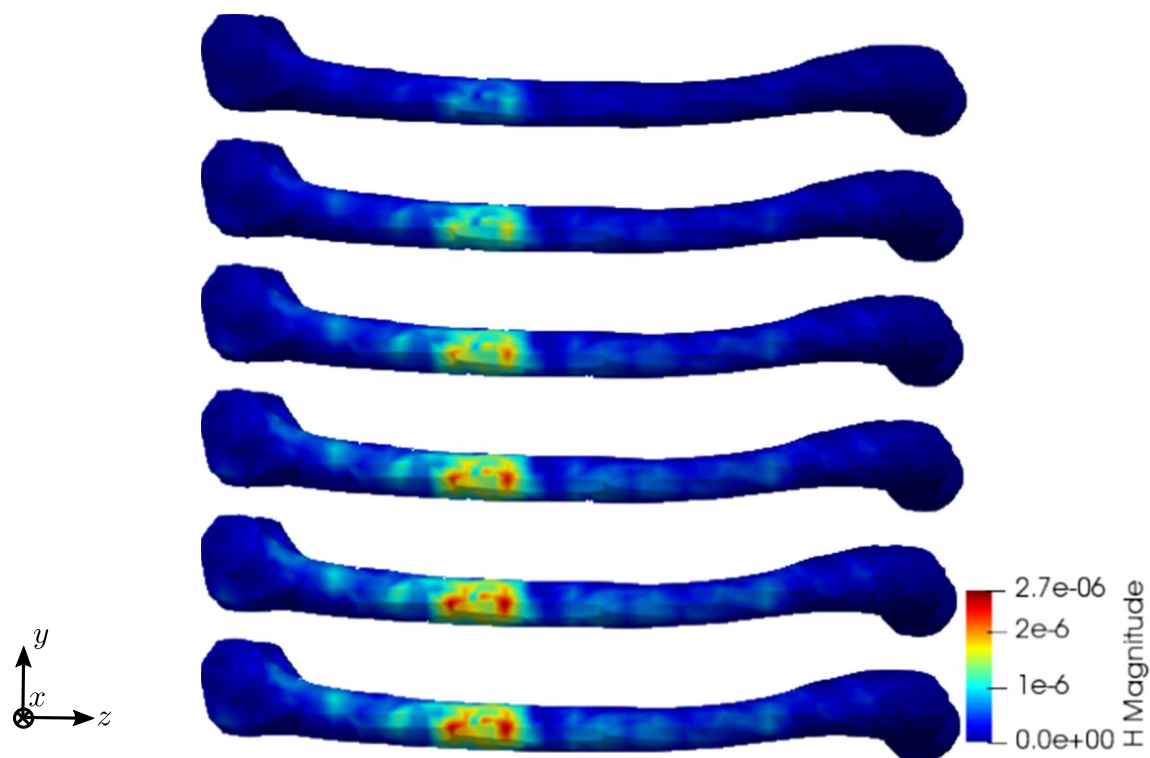


Fig. 26 Simulation results for RVE 1 (top) to 6 (bottom): magnitude of the magnetic field strength  $\mathbf{H}$  [A/m],  $t = 50$

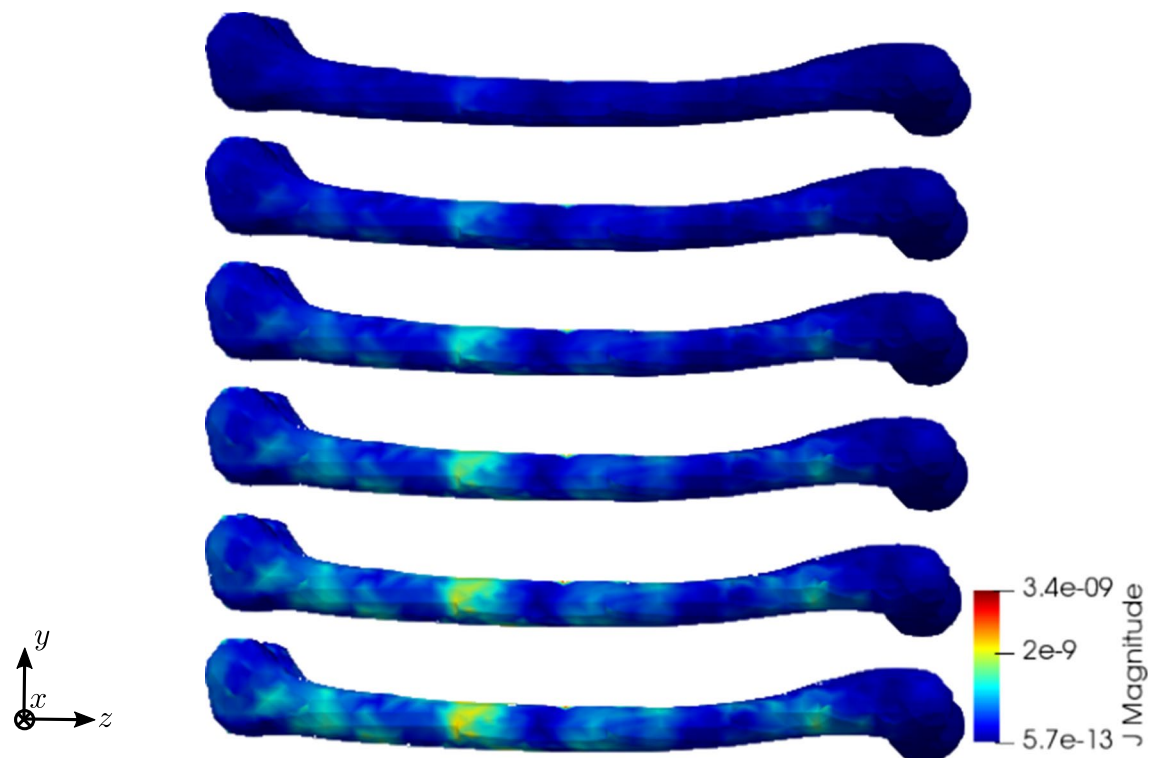
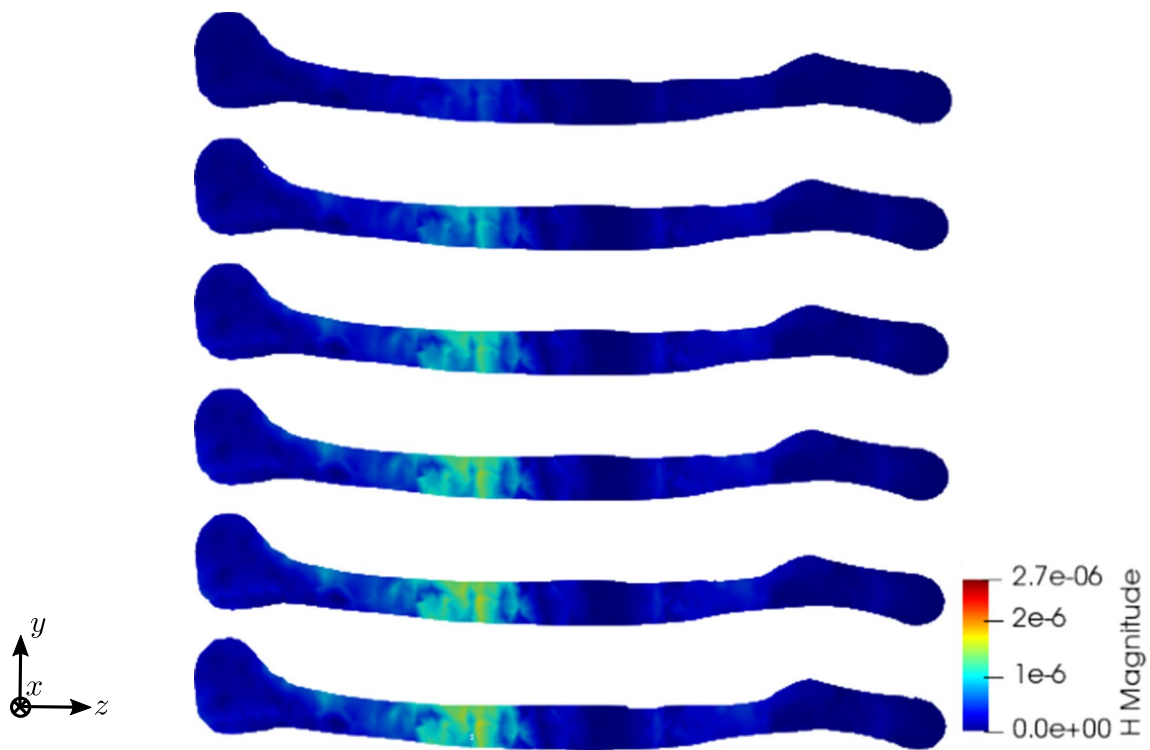
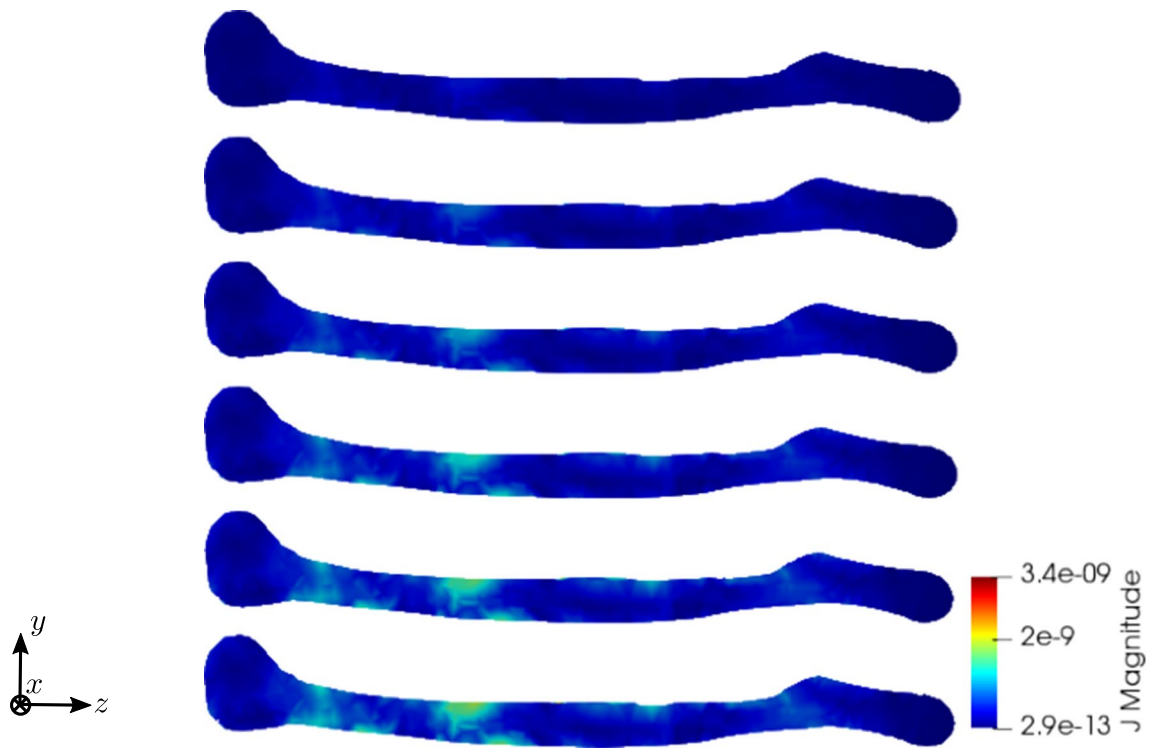


Fig. 27 Simulation results for RVE 1 (top) to 6 (bottom): magnitude of the electric current density  $\mathbf{J}$  [A/m<sup>2</sup>],  $t = 50$





**Fig. 28** Simulation results for RVE 1 (top) to 6 (bottom): magnitude of the magnetic field strength  $\mathbf{H}$  [A/m], slice,  $t = 50$



**Fig. 29** Simulation results for RVE 1 (top) to 6 (bottom): magnitude of the electric current density  $\mathbf{J}$  [A/m<sup>2</sup>], slice,  $t = 50$

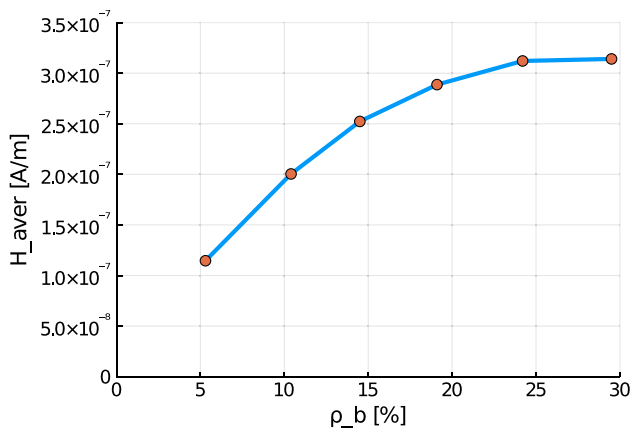


Fig. 30 Average magnetic field strength for the different RVEs at  $t = 50$

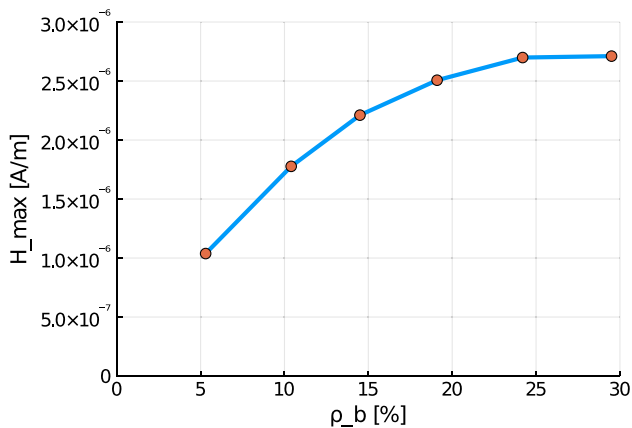


Fig. 31 Maximum magnetic field strength for the different RVEs at  $t = 50$

show again a similar behavior for all quantities. Between the two RVEs with the highest volume fraction of cortical bone phase, nearly no reduction of the magnetic field strength can be observed. With decreasing  $\rho_b$ , the differences grow increasingly larger. Compared to the healthy bone ( $\rho_b = 29.5\%$ ), the bone with late stage osteoporosis ( $\rho_b = 5.3\%$ ) shows a drastic reduction of the magnetic field strength by nearly two thirds. These results show, in which order of magnitude differences between healthy and degenerated bones can be expected, when performing experimental research and sonography for the purpose of early detection of osteoporosis.

For future research, we aim to solve the inverse problem by using an Artificial Neural Network to predict simulation outputs for random microstructures. Here, the network should recover the distribution of cortical bone phase in the macroscopic model from the magnetic field data, thus diagnosing the state of the bone. Additionally, wave

propagation in cancellous bone will be investigated in more detail. The comparison of experimental with simulation results could provide further insights. Accurate material parameters could be obtained from the experiments, which then could be used for the simulations. To make precise predictions for experimental setups, it is of great importance to address possible numerical problems of the simulations. The used RVEs have a very coarse mesh resolution and contain sharp edges. While our investigations so far show, that the coarse RVE with hexahedron elements performs best, it is still relevant to investigate in detail how the magnetic field strength is affected for different, smoother RVEs, which model the microstructure of bone in a more realistic way. Another important aspect is to investigate the microscale behavior for RVEs which differ in size and structure of the phases. Depending on the geometry of the used RVE, the simulation results can vary. Thus, for the future we plan to investigate this effect in detail. The usage of different function spaces could improve the results. Finally, our macroscopic models could be extended to include a surrounding medium like air or water, allowing proper decay of the magnetic field.

### Calculation of the strong form for the micro-problem

To calculate the strong form of the problem, we use the reduced weak form:

$$\int_{\Omega} (\boldsymbol{\sigma} \cdot \delta \boldsymbol{\varepsilon} - \mathbf{D} \cdot \delta \mathbf{E} + \mathbf{H} \cdot \delta \mathbf{B} - \mathbf{J} \cdot \delta \mathbf{A} + \gamma(\nabla \cdot \mathbf{A}) \cdot \delta(\nabla \cdot \mathbf{A})) dV - \delta W_{ext} = 0 \quad \forall \delta \mathbf{u}, \delta \varphi, \delta \mathbf{A} . \tag{50}$$

Now, we apply partial integration to each term followed by the use of a surface-volume integral rule:

$$\begin{aligned} \int_{\Omega} \boldsymbol{\sigma} \cdot \delta \boldsymbol{\varepsilon} dV &= \int_{\Omega} \nabla \cdot (\boldsymbol{\sigma} \cdot \delta \mathbf{u}) dV - \int_{\Omega} (\nabla \cdot \boldsymbol{\sigma}) \cdot \delta \mathbf{u} dV \\ &= \int_{\partial \Omega} \boldsymbol{\sigma} \cdot \mathbf{n} \cdot \delta \mathbf{u} dA - \int_{\Omega} (\nabla \cdot \boldsymbol{\sigma}) \cdot \delta \mathbf{u} dV, \end{aligned} \tag{51}$$

$$\begin{aligned}
 & \int_{t_0}^{t_1} \int_{\Omega} -\mathbf{D} \cdot \delta \mathbf{E} dV dt = \int_{t_0}^{t_1} \int_{\Omega} (\mathbf{D} \cdot \delta(\nabla \varphi) + \mathbf{D} \cdot \delta \dot{\mathbf{A}}) dV dt \\
 &= \int_{t_0}^{t_1} \int_{\Omega} \nabla \cdot (\mathbf{D} \delta \varphi) dV dt - \int_{t_0}^{t_1} \int_{\Omega} (\nabla \cdot \mathbf{D}) \delta \varphi dV dt \\
 & \quad - \int_{t_0}^{t_1} \int_{\Omega} \dot{\mathbf{D}} \cdot \delta \mathbf{A} dV dt + \underbrace{\int_{\Omega} [\mathbf{D} \cdot \delta \mathbf{A}]_{t_0}^{t_1} dV}_{=0} \\
 &= \int_{t_0}^{t_1} \int_{\partial \Omega} \mathbf{D} \cdot \mathbf{n} \delta \varphi dA dt - \int_{t_0}^{t_1} \int_{\Omega} (\nabla \cdot \mathbf{D}) \delta \varphi dV dt \\
 & \quad - \int_{t_0}^{t_1} \int_{\Omega} \dot{\mathbf{D}} \cdot \delta \mathbf{A} dV dt, \tag{52}
 \end{aligned}$$

$$\begin{aligned}
 \int_{\Omega} \mathbf{H} \cdot \delta \mathbf{B} dV &= \int_{\Omega} \nabla \cdot (\delta \mathbf{A} \times \mathbf{H}) dV + \int_{\Omega} \nabla \times \mathbf{H} \cdot \delta \mathbf{A} dV \\
 &= \int_{\partial \Omega} \mathbf{H} \times \mathbf{n} \cdot \delta \mathbf{A} dA + \int_{\Omega} \nabla \times \mathbf{H} \cdot \delta \mathbf{A} dV, \tag{53}
 \end{aligned}$$

$$\begin{aligned}
 & \int_{\Omega} \gamma(\nabla \cdot \mathbf{A}) \cdot \delta(\nabla \cdot \mathbf{A}) dV \\
 &= \int_{\Omega} \gamma \nabla \cdot ((\nabla \cdot \mathbf{A}) \cdot \delta \mathbf{A}) dV - \int_{\Omega} \gamma \nabla(\nabla \cdot \mathbf{A}) \delta \mathbf{A} dV \tag{54} \\
 &= \int_{\partial \Omega} \gamma(\nabla \cdot \mathbf{A}) \cdot \mathbf{n} \cdot \delta \mathbf{A} dA - \int_{\Omega} \gamma \nabla(\nabla \cdot \mathbf{A}) \delta \mathbf{A} dV.
 \end{aligned}$$

Here,  $\mathbf{n}$  is the normal vector pointing outwards. It should be noted that the term  $\mathbf{D} \cdot \delta \mathbf{A}$  in Eq. (52) vanishes, as the test function  $\delta \mathbf{A}$  does not change between the time  $t_0$  and  $t_1$ . For the magnetic energy variation Eq. (53), the sign is different compared to the other equations because of the cross product rule. Additionally, the resulting triple product in the surface integral allows cyclic permutation without changing the result. Inserting these identities in the reduced weak form Eq. (50) yields

$$\begin{aligned}
 & \int_{\Omega} (-\nabla \cdot \boldsymbol{\sigma} - \mathbf{f}) \cdot \delta \mathbf{u} dV + \int_{\partial \Omega} (\boldsymbol{\sigma} \cdot \mathbf{n} - \mathbf{t}) \cdot \delta \mathbf{u} dA \\
 &+ \int_{\Omega} (-\nabla \cdot \mathbf{D} + q_v) \cdot \delta \varphi dV + \int_{\partial \Omega} (\mathbf{D} \cdot \mathbf{n} + q_s) \cdot \delta \varphi dA \\
 & \quad + \int_{\Omega} (\nabla \times \mathbf{H} - \dot{\mathbf{D}} - \mathbf{J} - \gamma \nabla(\nabla \cdot \mathbf{A}) - \mathbf{j}_v) \cdot \delta \mathbf{A} dV \\
 &+ \int_{\partial \Omega} (\mathbf{H} \times \mathbf{n} - \mathbf{j}_s + \gamma(\nabla \cdot \mathbf{A}) \cdot \mathbf{n}) \cdot \delta \mathbf{A} dA = 0 \quad \forall \delta \mathbf{u}, \delta \varphi, \delta \mathbf{A}. \tag{55}
 \end{aligned}$$

Then, we calculate the strong form by using the arbitrariness of the test functions and by splitting the volume and surface of the area, resulting in Eq. (22) and the matching conditions Eq. (23).

### Derivation of the matrix form for the FEM

Inserting the FEM ansatz into the reduced weak form of the micro-problem Eq. (50) yields

$$\begin{aligned}
 & \int_{\Omega_b} ((\mathbf{C}_b \mathbf{B}_u \hat{\mathbf{u}} - \mathbf{e}_b^T [-\mathbf{B}_{\text{grad}} \hat{\boldsymbol{\varphi}} - \mathbf{N}_A \dot{\hat{\mathbf{A}}}] ) \mathbf{B}_u \delta \hat{\mathbf{u}} \\
 & - [\mathbf{e}_b \mathbf{B}_u \hat{\mathbf{u}} + \boldsymbol{\xi}_b (-\mathbf{B}_{\text{grad}} \hat{\boldsymbol{\varphi}} - \mathbf{N}_A \dot{\hat{\mathbf{A}}})] [-\mathbf{B}_{\text{grad}} \delta \hat{\boldsymbol{\varphi}} - \mathbf{N}_A \delta \dot{\hat{\mathbf{A}}}] \\
 & \quad + \mu_b^{-1} \mathbf{B}_{\text{curl}} \hat{\mathbf{A}} \mathbf{B}_{\text{curl}} \delta \hat{\mathbf{A}} + \gamma \mathbf{B}_{\text{div}} \mathbf{B}_{\text{div}}^T \delta \hat{\mathbf{A}}) dV \\
 & + \int_{\Omega_m} (\boldsymbol{\sigma}_m \mathbf{B}_u \delta \hat{\mathbf{u}} - [\boldsymbol{\xi}_m (-\mathbf{B}_{\text{grad}} \hat{\boldsymbol{\varphi}} - \mathbf{N}_A \dot{\hat{\mathbf{A}}})] [-\mathbf{B}_{\text{grad}} \delta \hat{\boldsymbol{\varphi}} \\
 & \quad - \mathbf{N}_A \delta \dot{\hat{\mathbf{A}}}] + \mu_m^{-1} \mathbf{B}_{\text{curl}} \hat{\mathbf{A}} \mathbf{B}_{\text{curl}} \delta \hat{\mathbf{A}} + \gamma \mathbf{B}_{\text{div}} \mathbf{B}_{\text{div}}^T \delta \hat{\mathbf{A}} \\
 & \quad - \boldsymbol{\kappa}_m [-\mathbf{B}_{\text{grad}} \hat{\boldsymbol{\varphi}} - \mathbf{N}_A \dot{\hat{\mathbf{A}}}] \mathbf{N}_A \delta \dot{\hat{\mathbf{A}}}) dV \\
 & \quad - \left( \int_{\Omega} \mathbf{N}_u^T \mathbf{f} dV + \int_{\partial \Omega} \mathbf{N}_u^T \mathbf{t} dA \right) \delta \hat{\mathbf{u}} \\
 & \quad + \left( \int_{\Omega} \mathbf{N}_{\varphi}^T q_v dV + \int_{\partial \Omega} \mathbf{N}_{\varphi}^T q_s dA \right) \delta \hat{\boldsymbol{\varphi}} \\
 & - \left( \int_{\Omega} \mathbf{N}_A^T \mathbf{j}_v dV + \int_{\partial \Omega} \mathbf{N}_A^T \mathbf{j}_s dA \right) \delta \hat{\mathbf{A}} = 0 \quad \forall \delta \hat{\mathbf{u}}, \delta \hat{\boldsymbol{\varphi}}, \delta \hat{\mathbf{A}}. \tag{56}
 \end{aligned}$$

Here, we use partial integration as follows:

$$\begin{aligned}
 & \int_{t_0}^{t_1} \int_{\Omega} \mathbf{N}_A^T \mathbf{e}_b \mathbf{B}_u \hat{\mathbf{u}} \delta \dot{\hat{\mathbf{A}}} dV dt \\
 &= \underbrace{\int_{\Omega} [\mathbf{N}_A^T \mathbf{e}_b \mathbf{B}_u \hat{\mathbf{u}} \delta \hat{\mathbf{A}}]_{t_0}^{t_1} dV}_{=0} - \int_{t_0}^{t_1} \int_{\Omega} \mathbf{N}_A^T \mathbf{e}_b \mathbf{B}_u \hat{\mathbf{u}} \delta \hat{\mathbf{A}} dV dt \tag{57}
 \end{aligned}$$

$$\int_{t_0}^{t_1} \int_{\Omega} \mathbf{N}_A^T \xi \mathbf{B}_{\text{grad}} \hat{\boldsymbol{\phi}} \delta \hat{\mathbf{A}} \, dV \, dt = \underbrace{\int_{\Omega} [\mathbf{N}_A^T \xi \mathbf{B}_{\text{grad}} \hat{\boldsymbol{\phi}} \delta \hat{\mathbf{A}}]_{t_0}^{t_1} \, dV}_{=0} - \int_{t_0}^{t_1} \int_{\Omega} \mathbf{N}_A^T \xi \mathbf{B}_{\text{grad}} \hat{\boldsymbol{\phi}} \delta \hat{\mathbf{A}} \, dV \, dt \tag{58}$$

$$\int_{t_0}^{t_1} \int_{\Omega} \mathbf{N}_A^T \xi \mathbf{N}_A \dot{\mathbf{A}} \delta \dot{\mathbf{A}} \, dV \, dt = \underbrace{\int_{\Omega} [\mathbf{N}_A^T \xi \mathbf{N}_A \dot{\mathbf{A}} \delta \dot{\mathbf{A}}]_{t_0}^{t_1} \, dV}_{=0} - \int_{t_0}^{t_1} \int_{\Omega} \mathbf{N}_A^T \xi \mathbf{N}_A \ddot{\mathbf{A}} \delta \dot{\mathbf{A}} \, dV \, dt \tag{59}$$

Again, the nodal test function  $\delta \hat{\mathbf{A}}$  does not change in time, so the corresponding terms vanish. Inserting this into Eq. (56) yields

$$\begin{aligned} & \int_{\Omega_b} ((\mathbf{C}_b \mathbf{B}_u \hat{\mathbf{u}} - \mathbf{e}_b^T [-\mathbf{B}_{\text{grad}} \hat{\boldsymbol{\phi}} - \mathbf{N}_A \dot{\mathbf{A}}]) \mathbf{B}_u \delta \hat{\mathbf{u}} \\ & - [\mathbf{e}_b \mathbf{B}_u \hat{\mathbf{u}} + \xi_b (-\mathbf{B}_{\text{grad}} \hat{\boldsymbol{\phi}} - \mathbf{N}_A \dot{\mathbf{A}})] [-\mathbf{B}_{\text{grad}} \delta \hat{\boldsymbol{\phi}}] \\ & + [\mathbf{e}_b \mathbf{B}_u \hat{\mathbf{u}} + \xi_b (-\mathbf{B}_{\text{grad}} \hat{\boldsymbol{\phi}} - \mathbf{N}_A \dot{\mathbf{A}})] [-\mathbf{N}_A \delta \hat{\mathbf{A}}] \\ & + \mu_b^{-1} \mathbf{B}_{\text{curl}} \hat{\mathbf{A}} \mathbf{B}_{\text{curl}} \delta \hat{\mathbf{A}} + \gamma \mathbf{B}_{\text{div}} \mathbf{B}_{\text{div}}^T \delta \hat{\mathbf{A}}) \, dV \\ & + \int_{\Omega_m} (\mathbf{B}_u^T \mathbf{C}_{\text{tang}} \mathbf{B}_u \delta \hat{\mathbf{u}} - [\xi_m (-\mathbf{B}_{\text{grad}} \hat{\boldsymbol{\phi}} - \mathbf{N}_A \dot{\mathbf{A}})] [-\mathbf{B}_{\text{grad}} \delta \hat{\boldsymbol{\phi}}] \\ & + [\xi_m (-\mathbf{B}_{\text{grad}} \hat{\boldsymbol{\phi}} - \mathbf{N}_A \dot{\mathbf{A}})] [-\mathbf{N}_A \delta \hat{\mathbf{A}}] + \mu_m^{-1} \mathbf{B}_{\text{curl}} \hat{\mathbf{A}} \mathbf{B}_{\text{curl}} \delta \hat{\mathbf{A}} \\ & + \gamma \mathbf{B}_{\text{div}} \mathbf{B}_{\text{div}}^T \delta \hat{\mathbf{A}} - \kappa_m [-\mathbf{B}_{\text{grad}} \hat{\boldsymbol{\phi}} - \mathbf{N}_A \dot{\mathbf{A}}] \mathbf{N}_A \delta \hat{\mathbf{A}}) \, dV \\ & - \left( \int_{\Omega} \mathbf{N}_u^T \mathbf{f} \, dV + \int_{\partial \Omega} \mathbf{N}_u^T \mathbf{t} \, dA \right) \delta \hat{\mathbf{u}} \\ & + \left( \int_{\Omega} \mathbf{N}_{\varphi}^T q_v \, dV + \int_{\partial \Omega} \mathbf{N}_{\varphi}^T q_s \, dA \right) \delta \hat{\boldsymbol{\phi}} \\ & - \left( \int_{\Omega} \mathbf{N}_A^T \mathbf{j}_v \, dV + \int_{\partial \Omega} \mathbf{N}_A^T \mathbf{j}_s \, dA \right) \delta \hat{\mathbf{A}} = 0 \, \forall \delta \hat{\mathbf{u}}, \delta \hat{\boldsymbol{\phi}}, \delta \hat{\mathbf{A}}. \end{aligned} \tag{60}$$

This equation can be split by the variations. By using the arbitrariness of the test functions and introducing the generalized nodal forces as

$$\begin{pmatrix} \hat{\mathbf{f}} \\ \hat{\mathbf{q}} \\ \hat{\mathbf{j}} \end{pmatrix} := \begin{pmatrix} \int_{\Omega} \mathbf{N}_u^T \mathbf{f} \, dV + \int_{\partial \Omega} \mathbf{N}_u^T \mathbf{t} \, dA \\ - \int_{\Omega} \mathbf{N}_{\varphi}^T q_v \, dV - \int_{\partial \Omega} \mathbf{N}_{\varphi}^T q_s \, dA \\ \int_{\Omega} \mathbf{N}_A^T \mathbf{j}_v \, dV + \int_{\partial \Omega} \mathbf{N}_A^T \mathbf{j}_s \, dA \end{pmatrix}, \tag{61}$$

the residual is then  $\mathbf{R} = (\mathbf{R}_u \, \mathbf{R}_{\varphi} \, \mathbf{R}_A)^T =$

$$\begin{pmatrix} \hat{\mathbf{f}} + \int_{\Omega} -\mathbf{B}_u^T \hat{\boldsymbol{\sigma}} \, dV \\ \hat{\mathbf{q}} + \int_{\Omega} -\mathbf{B}_{\text{grad}}^T \hat{\mathbf{D}} \, dV \\ \hat{\mathbf{j}} + \int_{\Omega} (-\mathbf{B}_{\text{curl}}^T \hat{\mathbf{H}} + \mathbf{N}_A^T (\hat{\mathbf{D}} + \hat{\mathbf{J}}) - \gamma \mathbf{B}_{\text{div}} \mathbf{B}_{\text{div}}^T \hat{\mathbf{A}}) \, dV \end{pmatrix} \tag{62}$$

By writing this equation in matrix form, we recover the equation system Eq. (32).

**Funding** Open Access funding enabled and organized by Projekt DEAL.

**Open Access** This article is licensed under a Creative Commons Attribution 4.0 International License, which permits use, sharing, adaptation, distribution and reproduction in any medium or format, as long as you give appropriate credit to the original author(s) and the source, provide a link to the Creative Commons licence, and indicate if changes were made. The images or other third party material in this article are included in the article's Creative Commons licence, unless indicated otherwise in a credit line to the material. If material is not included in the article's Creative Commons licence and your intended use is not permitted by statutory regulation or exceeds the permitted use, you will need to obtain permission directly from the copyright holder. To view a copy of this licence, visit <http://creativecommons.org/licenses/by/4.0/>.

**References**

Biot MA (1956) Theory of propagation of elastic waves in a fluid-saturated porous solid. I. Low-frequency range. *J Acoust Soc Am* 28(2):168–178

Biot MA (1956) Theory of propagation of elastic waves in a fluid-saturated porous solid. II. higher frequency range. *J Acoust Soc Am* 28(2):179–191

Blender (2021) <https://www.blender.org/>

Buchanan J, Gilbert RP (2007) Determination of the parameters of cancellous bone using high frequency acoustic measurements II: inverse problems. *Math Comput Model* 45:281–308

Carlsson K, Ekre F (2021) Juafem: jl a simple finite element toolbox written in julia

Castañeda PP, Suquet P (1997) Nonlinear composites. *Adv Appl Mech* 34:171–302

Chen H, Gilbert RP, Guyenne P (2018) A biot model for the determination of material parameters of cancellous bone from acoustic measurements. *Inverse Prob* 34(8):085009

Christen D, Webster DJ, Müller R (2010) Multiscale modelling and nonlinear finite element analysis as clinical tools for the assessment of fracture risk. *Philos Trans R Soc A Math Phys Eng Sci* 368(1920):2653–2668

de Diego A, Junge O, Karrasch D, Schilling N (2021) Coherentstructures.jl: tools for computing lagrangian coherent structures in julia

Fukada E, Yasuda I (1957) On the piezoelectric effect of bone. *J Phys Soc Jpn* 12(10):1158–1162

- Gardner T, Stoll T, Marks L, Mishra S (2000) The influence of mechanical stimulus on the pattern of tissue differentiation in a long bone fracture: an fem study. *J Biomech* 33(415–25):05
- Geuzaine C, Remacle JF (2021) Gmsh: a three-dimensional finite element mesh generator with built-in pre- and post-processing facilities
- Güzelsu N, Saha S (1981) Electro-mechanical wave propagation in long bones. *J Biomech* 14(1):19–33
- Hamed E, Lee Y, Jasiuk I (2010) Multiscale modeling of elastic properties of cortical bone. *Acta Mech* 213(1):131–154
- Hill R (1963) Elastic properties of reinforced solids: Some theoretical principles. *J Mech Phys Solids* 11(5):357–372
- Hill R (1972) On constitutive macro-variables for heterogeneous solids at finite strain. *Proc R Soc Lond A Math Phys Sci* 326(1565):131–147
- Ilić S, Hackl K (2004) Homogenisation of random composites via the multiscale finite-element method. *PAMM* 4(1):326–327
- Ilic S, Hackl K, Gilbert RP (2010) Application of the multiscale fem to the modeling of cancellous bone. *Biomech Model Mechanobiol* 9(1):87–102
- Kadapa C, Dettmer W, Perić D (2017) On the advantages of using the first-order generalised-alpha scheme for structural dynamic problems. *Comput Struct* 193:12
- Karimi P, Zhang X, Yan S, Ostoja-Starzewski M, Jin JM (2019) Electrostatic and magnetostatic properties of random materials. *Phys Rev E* 99:022120
- Kaufman JJ, Luo G, Siffert RS (2008) Ultrasound simulation in bone. *IEEE Trans Ultrason Ferroelectr Freq Control* 55(6):1205–1218
- Klinge S, Hackl K, Gilbert RP (2013) Investigation of the influence of reflection on the attenuation of cancellous bone. *Biomech Model Mechanobiol* 12:185–199
- Krylovmethods (2021) Krylovmethods.jl: Simple and fast julia implementation of krylov subspace methods for linear systems
- Laboratoires Servier (2019) Osteoporosis
- Labusch M, Schröder J, Lupascu DC (2019) A two-scale homogenization analysis of porous magneto-electric two-phase composites. *Arch Appl Mech*
- Lifescience database (2021) <https://lifesciencedb.jp/bp3d/>
- Mehrabadi MM, Cowin SC (1990) Eigensensors of linear anisotropic elastic materials. *Quart J Mech Appl Math* 43(1):15–41:02
- Miehe C, Schotte J, Lambrecht M (2002) Homogenization of inelastic solid materials at finite strains based on incremental minimization principles. application to the texture analysis of polycrystals. *J Mech Phys Solids* 50(10):2123–2167
- Miller Z, Fuchs M, Arcan M (2002) Trabecular bone adaptation with an orthotropic material model. *J Biomech* 35(247–56):03
- Mohammadkhah M, Marinkovic D, Zehn M, Checa S (2019) A review on computer modeling of bone piezoelectricity and its application to bone adaptation and regeneration. *Bone* 127:544–555
- Pahr DH, Zysset PK (2008) Influence of boundary conditions on computed apparent elastic properties of cancellous bone. *Biomech Model Mechanobiol* 7(6):463–476
- Paraview (2021) <https://www.paraview.org/>
- Podshivalov L, Fischer A, Bar-Yoseph PZ (2011) Multiscale fe method for analysis of bone micro-structures. *J Mech Behav Biomed Mater* 4(6):888–899
- Schröder J (2000) Homogenisierungsmethoden der nichtlinearen Kontinuumsmechanik unter Beachtung von Instabilitäten. Institut für Mechanik (Bauwesen). In: Lehrstuhl I (ed) Habilitationsschrift. Universität Stuttgart, Stuttgart
- Schröder J (2009) Derivation of the localization and homogenization conditions for electro-mechanically coupled problems. *Comput Mater Sci* 46:595–599
- Schröder J, Labusch M, Keip MA (2016) Algorithmic two-scale transition for magneto-electro-mechanically coupled problems: Fe2-scheme: Localization and homogenization. *Comput Methods Appl Mech Eng* 302:253–280
- Schröder J, Hackl K (2013) Plasticity and Beyond: Microstructures. Crystal-Plasticity and Phase Transitions. CISM International Centre for Mechanical Sciences, Springer Vienna
- Semenov AS, Kessler H, Liskowsky A, Balke H (2006) On a vector potential formulation for 3D electromechanical finite element analysis. *Commun Numer Methods Eng* 22(5):357–375
- Shamos MH, Lavine LS, Shamos MI (1963) Piezoelectric effect in bone. *Nature* 197(4862):81–81
- Steeb H (2010) Ultrasound propagation in cancellous bone. *Arch Appl Mech* 80(5):489–502
- Suquet P (1987) Elements of homogenization theory for inelastic solid mechanics, in homogenization techniques for composite media
- The julia programming language (2021). <https://julialang.org/>
- Ural A, Mischinski S (2013) Multiscale modeling of bone fracture using cohesive finite elements. *Eng Fract Mech* 103:141–152. *Advances in Failure Assessment Using Fracture and Damage Mechanics*
- Wang L, Zhang J, Zhang W, Yang H-L, Luo Z-P (2017) Analysis of the osteogenic effects of biomaterials using numerical simulation. *BioMed Res Int*, 2017:6981586–6981586, 28116309[pmid]
- Willis JR (1981) Variational and related methods for the overall properties of composites. *Adv Appl Mech* 21:1–78
- Zienkiewicz OC, Taylor RL, Zhu JZ (2005) *The finite element method: its basis and fundamentals*, 6th edn. Butterworth-Heinemann, Oxford

**Publisher's Note** Springer Nature remains neutral with regard to jurisdictional claims in published maps and institutional affiliations.